Ocean Modelling 61 (2013) 21–37

Contents lists available at SciVerse ScienceDirect

Ocean Modelling

journal homepage: www.elsevier.com/locate/ocemod

Review

Detection of spatio-temporal wave grouping properties by using temporal sequences of X-band radar images of the sea surface

J.C. Nieto Borge [a,*], K. Reichert [b], K. Hessner [c]

[a] Dpt. of Signal Theory and Communications, Escuela Politécnica Superior, Universidad de Alcalá, Campus Universitario s/n, 28805 Alcalá de Henares, Madrid, Spain
[b] OceanWaveS Pacific Ltd., 23 Corrondella Grove, 5010 Lower Hutt, New Zealand
[c] OceanWaveS GmbH, Hansekontor, Vor dem Bardowicker Tore 6b, D-21339 Lüneburg, Germany

A R T I C L E I N F O

Article history:
Received 28 May 2012
Received in revised form 7 October 2012
Accepted 10 October 2012
Available online 2 November 2012

Keywords:
Wind-generated waves
Wave grouping
X-band radar
Remote sensing

A B S T R A C T

This work analyses wave groupiness features in the three-dimensional spatio-temporal domain by using sea surface information acquired by common X-band marine radars. The analysis is based on the study of the properties of the local and instantaneous envelope derived from wave elevation fields estimated from time series of radar images of the sea surface. The consistence of the analysis techniques proposed in this work are compared with standard one-dimensional wave grouping methods, such as the temporal correlation between consecutive wave heights. These comparisons are carried out using simulations of sea surfaces based on the stochastic description of sea states.

Contents

1. Introduction

It is a well known fact that wind-generated waves propagate in the ocean in sequences of contiguous high waves with nearly equal periods (Longuet-Higgins, 1984; Goda, 2010). This phenomenon is commonly named as wave grouping. These groups of waves are specially dangerous for the safety of marine systems, such as moving ships, off-shore platforms, coastal structures, etc., because the periods involved in those groups can cause effects of mechanical resonance when they are close to the motion or vibration periods of the marine systems (Clauss et al., 2008). The physical explanation of the wave grouping phenomenon is not yet fully clarified

* Corresponding author. Tel.: +34 918856654; fax: +34 918856699.
E-mail addresses: josecarlos.nieto@uah.es (J.C. Nieto Borge), kreichert@oceanwaves-pacific.co.nz (K. Reichert), hessner@oceanwaves.de (K. Hessner).

1463-5003/$ - see front matter © 2012 Elsevier Ltd. All rights reserved.
http://dx.doi.org/10.1016/j.ocemod.2012.10.004

(Mollo-Christensen and Ramamonjiariosa, 1980; Ochi, 2005). Traditionally, wave grouping features have been characterized in the temporal domain t from wave elevation time series acquired by in situ-sensors (i.e. anchored buoys, wave lasers, etc.) moored at a fixed position (Hamilton et al., 1979; Medina and Hudspeth, 1990; Donelan et al., 1996). Alternatively to those point measurements, in the recent years different remote sensing techniques capable of studying the sea surface in space and time have been developed. Some of these techniques are based on the use of passive sensors, like video cameras (Piotrowski and Dugan, 2002; Gallego et al., 2011; Benetazzo et al., 2012). For instance, other techniques use active microwave sensors, such as incoherent and coherent radars mounted on off- and on-shore stations or moving vessels (Ziemer and Dittmer, 1994; Buckley et al., 1994; Buckley and Aler, 1997, 1998; Nieto-Borge et al., 1999; Trizna, 2001; Ziemer et al., 2004; Bell et al., 2005; Wu et al., 2011). All those remote sensing techniques are able to acquire temporal sequences of images of the sea surface. Hence, the evolution of sea surface can be analyzed in the two spatial coordinates that define the mean level of the sea surface $\mathbf{r} = (x, y)$ and time t.

This work deals with the analysis of wave grouping properties in space and time by using time series of X-band marine radar images of the sea surface. Some previous works has been carried out to analyze wave grouping properties from space-borne SAR images, as well as temporal sequences of marine radar images (Dankert et al., 2003), where the analysis of wave groups is derived from estimations of the wave envelope obtained from Gabor filtering techniques. As an alternative, this paper estimates the wave envelope in the spatio-temporal domain using a technique based on the Riesz Transform (King, 2009b), which is closely related to dynamical features of the wave field evolution. For that purpose, the Riesz Transform is applied to estimations of the sea surface elevation field $\eta(x, y, t)$ scanned by X-band marine radars by using inversion modeling techniques (Nieto-Borge et al., 2004b; Terrill and de, 2009). Although, this work uses the wave elevation fields derived from the X-band marine radar analysis, the methods described in this paper are suitable to be applied to any measurement of the wave elevation field in space $\mathbf{r} = (x, y)$ and time t retrieved from other sensors capable to scan areas of the sea surface for different time steps.

The paper is structured as follow: Sections 2 and 3 describes the theoretical background used in this work to analyze wave grouping properties in the three-dimensional spatio-temporal domain (x, y, t). The following Section 4 introduces briefly the methodology to analyze wave fields by using marine radars. This section describes as well the inversion modeling technique to estimate the wave elevation field $\eta(x, y, t)$ from the marine radar data sets. Section 5 shows the results of the wave grouping detection derived from records acquired by a wave measuring station based on X-band marine radar technology. The consistence of the techniques used in this work are compared with standard one-dimensional wave grouping analysis method using stochastic simulations of sea surfaces. This comparison is shown in Section 6. Finally, Section 7 deals with the conclusions of the work.

2. Theoretical background

Under the frame of the linear wave theory the Eulerian description of the wave elevation η at a position $\mathbf{r} = (x, y)$ of the sea surface and at time t is regarded as a superposition of different monochromatic wave components (Ochi, 2005; Krogstad and Trulsen, 2010). Hence, using a discrete notation, $\eta(\mathbf{r}, t)$ can be expressed as

$$\eta(\mathbf{r}, t) = \sum_m a_m \cos(\mathbf{k}_m \cdot \mathbf{r} - \omega_m t + \varphi_m), \tag{1}$$

where the index m denotes the mth-wave spectral component that is characterized by its amplitude a_m, wave number vector $\mathbf{k}_m = (k_{x_m}, k_{y_m})$, angular frequency ω_m and phase φ_m. The different wave numbers $\mathbf{k}_1, \mathbf{k}_2, \ldots$ and frequencies $\omega_1, \omega_2, \ldots$ are non-harmonic. Wave fields given by the expression (1) are considered as zero-mean Gaussian stochastic process, where the spectral components are statistically independent, being a_m and φ_m random variables. The wave field representation given by Eq. (1) is appropriate for sea state conditions (Goda, 2010), where the free wave components of the surface do not change in space and time (e.g. statistical temporal stationarity and spatial homogeneity are assumed). Furthermore, as Eq. (1) represents a Gaussian process, this model describes wave fields with statistical symmetry between wave crests and troughs. In that case, the amplitudes a_m are derived from the linear wave spectrum (Fedele et al., 2011b; Krogstad and Trulsen, 2010), which do not take into account high-order nonlinear contributions (Tayfun and Fedele, 2007; Fedele et al., 2011c). In the following, all the spectra used in the text correspond to linear spectra consistent with the first-order description of wave fields given by Eq. (1). Under these conditions, the variance of $\eta(\mathbf{r}, t)$ is given by

$$\sigma^2 = \overline{\eta^2} = \frac{1}{2}\sum_m \overline{a_m^2} = m_0 \tag{2}$$

where the overline denotes the mean value, and m_0 indicates the 0th-order moment, which is commonly estimated from the wave spectrum.

2.1. Wave groups and local and instantaneous energy

Wave groupiness is related to the wave energy propagation. Those phenomena are proportional to the square of η. Hence, the local and instantaneous potential wave energy per unit of area $E_p(\mathbf{r}, t)$ is related to η^2 as (Gran, 1992)

$$E_p(\mathbf{r}, t) = \frac{1}{2}\rho g \eta^2(\mathbf{r}, t) \tag{3}$$

where ρ is the density of the sea water and g the acceleration of the gravity. From Eq. (1), $\eta^2(\mathbf{r}, t)$ can be expressed as (Massel, 1996)

$$\eta^2(\mathbf{r}, t) = \frac{1}{2}[G(\mathbf{r}, t) + P(\mathbf{r}, t)], \tag{4}$$

where $G(\mathbf{r}, t)$ and $P(\mathbf{r}, t)$ are known as group train and pulse train respectively (Gran, 1992). These magnitudes are given by

$$G(\mathbf{r}, t) = \sum_m \sum_n a_m a_n \times \cos[(\mathbf{k}_m - \mathbf{k}_n)\cdot\mathbf{r} - (\omega_m - \omega_n)t + \varphi_m - \varphi_n], \tag{5}$$

and

$$P(\mathbf{r}, t) = \sum_m \sum_n a_m a_n \times \cos[(\mathbf{k}_m + \mathbf{k}_n)\cdot\mathbf{r} - (\omega_m + \omega_n)t + \varphi_m + \varphi_n]. \tag{6}$$

Eqs. (5) and (6) show that $G(\mathbf{r}, t)$ and $P(\mathbf{r}, t)$ contain second-order spectral contributions of the wave field $\eta(\mathbf{r}, t)$ given by Eq. (1). Eq. (5) indicates that $G(\mathbf{r}, t)$ contains the spectral contributions of low frequencies $\omega_m - \omega_n$ and low wave numbers $\mathbf{k}_m - \mathbf{k}_n$. Therefore, $G(\mathbf{r}, t)$ is responsible of the wave energy propagation for long scales in time and space. The velocity of these spectral components are given by

$$\frac{\omega_m - \omega_n}{|\mathbf{k}_m - \mathbf{k}_n|} \approx \frac{d\omega}{dk}, \tag{7}$$

which is the group velocity. Eq. (6) indicates that the spectral components of the pulse train $P(\mathbf{r}, t)$ correspond to short scale evolution in time and space of the wave energy propagation.

Assuming that the wave spectral components of the wave elevation field $\eta(\mathbf{r}, t)$ are statistically independent, and taking into account Eqs. (5) and (6), the spatial and temporal ensemble averages of $G(\mathbf{r}, t)$ and $P(\mathbf{r}, t)$ are respectively

$$\overline{G(\mathbf{r}, t)} = \sum_m \overline{a_m^2} = 2m_0, \tag{8}$$

$$\overline{P(\mathbf{r}, t)} = 0. \tag{9}$$

Therefore, under the theoretical assumptions described above, only the group train contains the information of the propagation of averaged wave energy. Taking into account Eq. (4) the local and instantaneous potential energy per unit of area takes the form

$$E_p(\mathbf{r}, t) = \frac{1}{4}\rho g[G(\mathbf{r}, t) + P(\mathbf{r}, t)]. \tag{10}$$

The local and instantaneous kinetic wave energy $E_k(\mathbf{r}, t)$ per unit of area can be computed as well. From Eq. (1), and assuming the linear wave theory, the local and instantaneous kinetic energy per unit of area is obtained by integrating the squared modulus of the orbital velocity (u, v, w) over all the water depth column (Gran, 1992)

$$E_k(\mathbf{r}, t) = \frac{1}{2}\rho \int_{-h}^{0} \left[u^2(\mathbf{r}, z, t) + v^2(\mathbf{r}, z, t) + w^2(\mathbf{r}, z, t)\right] dz, \tag{11}$$

where h is the water depth, $u(\mathbf{r}, z, t)$, $v(\mathbf{r}, z, t)$, and $w(\mathbf{r}, z, t)$ are the three components of the orbital velocity of the water particles at depth z $(-h \leqslant z \leqslant 0)$ (Massel, 1996)

$$u(\mathbf{r}, z, t) = -\sum_m c_m(z) a_m \omega_m \frac{k_{x_m}}{|\mathbf{k}_m|} \cos(\mathbf{k}_m \cdot \mathbf{r} - \omega_m t + \varphi_m) \tag{12}$$

$$v(\mathbf{r}, z, t) = -\sum_m c_m(z) a_m \omega_m \frac{k_{y_m}}{|\mathbf{k}_m|} \cos(\mathbf{k}_m \cdot \mathbf{r} - \omega_m t + \varphi_m) \tag{13}$$

$$w(\mathbf{r}, z, t) = \sum_m s_m(z) a_m \omega_m \sin(\mathbf{k}_m \cdot \mathbf{r} - \omega_m t + \varphi_m) \tag{14}$$

where $c_m(z) \equiv \frac{\cosh[k_m(h+z)]}{\cosh(k_m h)}$, and $s_m(z) \equiv \frac{\sinh[k_m(h+z)]}{\sinh(k_m h)}$. In first approach, taking into account only the contributions of those wave components traveling close to the mean wave propagation direction (e.g. long crest approach), and assuming deep water conditions $(h \to \infty)$, Eq. (11) is approached as (Gran, 1992)

$$E_k(\mathbf{r}, t) \approx \frac{1}{4}\rho g G(\mathbf{r}, t) \tag{15}$$

where the dispersion relation for linear waves in deep waters $\omega_m^2 = g|\mathbf{k}_m|$ has been taking into account. Hence, the local and instantaneous total wave energy per unit of area $E(\mathbf{r}, t)$ is given by

$$E(\mathbf{r}, t) = E_p(\mathbf{r}, t) + E_k(\mathbf{r}, t) \approx \frac{1}{2}\rho g\left[G(\mathbf{r}, t) + \frac{1}{2}P(\mathbf{r}, t)\right] \tag{16}$$

The equipartition of energy in Eq. (16) is a consequence of assuming a linear wave field shown in Eq. (1). The total energy per unit of area is a constant given by the ensemble spatio-temporal average $\overline{E(\mathbf{r}, t)} = \rho g m_0$.

All these wave energy expressions shown above depend on the determination of the group and pulse trains. In practice, due to the complexity of the calculations, the magnitudes $G(\mathbf{r}, t)$ and $P(\mathbf{r}, t)$ are not determined respectively by using the bispectral expressions given by Eqs. (5) and (6). This analysis is easily carried out by the estimation of the wave envelope, which is the subject of the following sections.

2.2. Relation between wave envelope and the local and instantaneous wave energy

Wave energy propagation can be determined towards the so-called wave envelope. Assuming the wave elevation η is a narrow banded process, the expression (1) can be factorized using a characteristic wave number $\mathbf{k}_c$ and frequency ω_c (Goda, 2010). These parameters are usually identified with the mean wave number vector and the mean frequency of the wave field, which are estimated respectively from the directional wave number spectral density $F(\mathbf{k})$ and the frequency spectral density $S(\omega)$ of the wave elevation field $\eta(\mathbf{r}, t)$. Under these conditions, Eq. (1) can be rewritten as

$$\eta(\mathbf{r}, t) = \eta_c(\mathbf{r}, t)\cos(\mathbf{k}_c \cdot \mathbf{r} - \omega_c t) - \eta_s(\mathbf{r}, t)\sin(\mathbf{k}_c \cdot \mathbf{r} - \omega_c t) \tag{17}$$

where

$$\eta_c(\mathbf{r}, t) = \sum_m a_m \cos[(\mathbf{k}_m - \mathbf{k}_c) \cdot \mathbf{r} - (\omega_m - \omega_c)t + \varphi_m] \tag{18}$$

and

$$\eta_s(\mathbf{r}, t) = \sum_m a_m \sin[(\mathbf{k}_m - \mathbf{k}_c) \cdot \mathbf{r} - (\omega_m - \omega_c)t + \varphi_m]. \tag{19}$$

Defining the variables

$$A(\mathbf{r}, t) \equiv \sqrt{\eta_c^2(\mathbf{r}, t) + \eta_s^2(\mathbf{r}, t)}, \tag{20}$$

$$\phi(\mathbf{r}, t) \equiv \tan^{-1}\left[\frac{\eta_s(\mathbf{r}, t)}{\eta_c(\mathbf{r}, t)}\right], \tag{21}$$

the quantities $\eta_c(\mathbf{r}, t)$ and $\eta_s(\mathbf{r}, t)$ are rewritten as

$$\eta_c(\mathbf{r}, t) = A(\mathbf{r}, t)\cos\phi(\mathbf{r}, t), \tag{22}$$

$$\eta_s(\mathbf{r}, t) = A(\mathbf{r}, t)\sin\phi(\mathbf{r}, t), \tag{23}$$

and the wave elevation field $\eta(\mathbf{r}, t)$ is expressed as

$$\eta(\mathbf{r}, t) = A(\mathbf{r}, t)\cos\Phi(\mathbf{r}, t) \tag{24}$$

where $\Phi(\mathbf{r}, t) \equiv \phi(\mathbf{r}, t) + \mathbf{k}_c \cdot \mathbf{r} - \omega_c t$. Eq. (24) indicates that $A(\mathbf{r}, t)$ is the local and instantaneous wave envelope, and $\Phi(\mathbf{r}, t)$ is the local and instantaneous phase. Taking into account Eq. (20), and the definitions given by Eqs. (18) and (19), it can be seen that

$$A^2(\mathbf{r}, t) = \eta_c^2(\mathbf{r}, t) + \eta_s^2(\mathbf{r}, t) = G(\mathbf{r}, t) \tag{25}$$

where $G(\mathbf{r}, t)$ is the group train given by Eq. (5). Knowing the wave envelope $A(\mathbf{r}, t)$ and the wave elevation field $\eta(\mathbf{r}, t)$, the pulse train $P(\mathbf{r}, t)$ is given by

$$P(\mathbf{r}, t) = 2\eta^2(\mathbf{r}, t) - A^2(\mathbf{r}, t). \tag{26}$$

It can be seen that, while $G(\mathbf{r}, t) = A^2(\mathbf{r}, t)$ takes always positive values, the pulse train $P(\mathbf{r}, t)$ can take positive or negative values depending on the relationship between the values of $2\eta^2(\mathbf{r}, t)$ and $A^2(\mathbf{r}, t)$.

2.3. Estimation of the wave envelope by using the Riesz Tansform

In practical cases the local and instantaneous wave envelope $A(\mathbf{r}, t)$ is not determined using the expression given by Eq. (20) introduced in Section 2.2. In the case of one-dimensional wave elevation fields (e.g. heave time series recorded by anchored buoys) the so-called instantaneous amplitude $A(t)$ is usually estimated by using the Hilbert transform (HT) (Medina and Hudspeth, 1990). For higher dimensions there is not a unique generalization of HT (Bülow et al., 2000; King, 2009b). All the different multidimensional generalizations of HT hold two main properties: the first one is that they coincide with the conventional HT for the one-dimensional case, the second one is that each generalization factorizes the original signal as an amplitude multiplied by the cosine of a phase as Eq. (24) shows. To compute the local and instantaneous amplitude $A(\mathbf{r},t)$ of the wave elevation field $\eta(\mathbf{r},t)$, this work uses the Riesz transform (RT) as multidimensional generalization of the HT. In the same way than the HT for the one-dimensional case, RT is related to the horizontal displacements of the water surface particles (Krogstad and Trulsen, 2010), which are as well used to derive the Lagrangian description of the sea surface elevation (Nouguier et al., 2009).

Hence, assuming the linear wave theory, the Riesz transform of $\eta(\mathbf{r},t)$ is closely related to the kinetic properties of the wave field evolution. For a given time t, the two-dimensional RT of the wave elevation field $\eta(\mathbf{r},t)$ is defined as (King, 2009b; Sierra-Vázquez and Serrano-Pedraza, 2010)

$$\hat{\eta}_j(\mathbf{r},t) = \frac{1}{2\pi}\lim_{\varepsilon\to 0}\int_{|\lambda|>\varepsilon}\eta(\mathbf{r},t)\frac{x_j-\lambda_j}{|\mathbf{r}-\boldsymbol{\lambda}|^3}d\lambda_1 d\lambda_2; \quad j=1,2; \tag{27}$$

where $\boldsymbol{\lambda}=(\lambda_1,\lambda_2)$. The index j takes the values $j=1$ or $j=2$ denoting the directions x and y respectively. From the two components of RT, $\hat{\eta}_x(\mathbf{r},t)\equiv\hat{\eta}_1(\mathbf{r},t)$ and $\hat{\eta}_y(\mathbf{r},t)\equiv\hat{\eta}_2(\mathbf{r},t)$, a vector field $\boldsymbol{\eta}(\mathbf{r},t)$ is constructed as (King, 2009b)

$$\boldsymbol{\eta}(\mathbf{r},t) = \left(\eta(\mathbf{r},t),\hat{\eta}_x(\mathbf{r},t),\hat{\eta}_y(\mathbf{r},t)\right)^T. \tag{28}$$

The estimation of the local and instantaneous amplitude $A(\mathbf{r},t)$ by using RT, $A_r(\mathbf{r},t)$, is obtained as the norm of the vector field $\boldsymbol{\eta}(\mathbf{r},t)$ (Bülow et al., 2000)

$$A_r(\mathbf{r},t) = |\boldsymbol{\eta}(\mathbf{r},t)| = \sqrt{\eta^2(\mathbf{r},t)+\hat{\eta}_x^2(\mathbf{r},t)+\hat{\eta}_y^2(\mathbf{r},t)}. \tag{29}$$

The respective RT estimation of the local and instantaneous phase $\Phi_r(\mathbf{r},t)$ is given by

$$\Phi_r(\mathbf{r},t) = \tan^{-1}\left[\frac{\sqrt{\hat{\eta}_x^2(\mathbf{r},t)+\hat{\eta}_y^2(\mathbf{r},t)}}{\eta(\mathbf{r},t)}\right]. \tag{30}$$

From Eq. (29) and (30), the wave elevation field η is derived as an equivalent expression than Eq. (24)

$$\eta(\mathbf{r},t) = A_r(\mathbf{r},t)\cos\Phi_r(\mathbf{r},t). \tag{31}$$

For practical cases, Eq. (27) is not applied and RT is computed by using the relationship between the Fourier transforms of the original signal η and its respective RT vector components (Sierra-Vázquez and Serrano-Pedraza, 2010)

$$\mathcal{F}[\hat{\eta}_j] = -i\frac{k_j}{|\mathbf{k}|}\mathcal{F}[\eta]; \quad j=1,2; \tag{32}$$

where $\mathcal{F}$ denotes the Fourier Transform, $i=\sqrt{-1}$, and k_1 and k_2 are the two components of the wave number vector $\mathbf{k}$ (e.g. $k_1\equiv k_x$, and $k_2\equiv k_y$). Taking into account Eq. (32), the two components of the Riesz transform of the wave elevation field $\eta(\mathbf{r},t)$ given by Eq. (1) are then given by

$$\hat{\eta}_x(\mathbf{r},t) = \sum_m a_m\frac{k_{x_m}}{|\mathbf{k}_m|}\sin(\mathbf{k}_m\cdot\mathbf{r}-\omega_m t+\varphi_m) \tag{33}$$

$$\hat{\eta}_y(\mathbf{r},t) = \sum_m a_m\frac{k_{y_m}}{|\mathbf{k}_m|}\sin(\mathbf{k}_m\cdot\mathbf{r}-\omega_m t+\varphi_m) \tag{34}$$

At it was mentioned before, Eqs. (33) and (34) correspond to the horizontal wave displacements at the mean sea surface (e.g. $z=0$) (Krogstad and Trulsen, 2010). Therefore, the horizontal orbital velocity components (u,v) at $z=0$ can be derived from the partial derivative in time of $\hat{\eta}_x$ and $\hat{\eta}_y$ respectively (see Eqs. (12) and (13)).

Knowing the RT components $\hat{\eta}_x(\mathbf{r},t)$ and $\hat{\eta}_y(\mathbf{r},t)$, the local and instantaneous wave envelope is estimated using Eq. (29) (Nieto-Borge et al., 2010). Hence, the group and pulse train are as well estimated by applying Eqs. (25) and (26), and, therefore, the potential, kinetic and total wave energies per unit of area can be as well estimated by using Eqs. (10), (15), and (16) respectively.

Apart of the estimation of the wave energy features, the wave envelope $A(\mathbf{r},\mathbf{t})$ permits as well to estimate local and instantaneous properties of the wave height. Hence, assuming that the wave elevation field $\eta(\mathbf{r},t)$ is a Gaussian process, the probability density function of the envelope $A(\mathbf{r},t)$ process follows a Rayleigh distribution (Longuet-Higgins, 1984, 1986). Therefore, considering that the wave elevation $\eta(\mathbf{r},t)$ is a narrow-banded process, the probability that the maxima of $\eta(\mathbf{r},\mathbf{t})$ are located elsewhere than the wave crests is small (Ochi, 2005). Hence, $A(\mathbf{r},t)$ is strongly correlated with the amplitudes of the individual wave heights. In addition, for narrow-banded processes, there is a statistical symmetry for crests and troughs. Therefore, the wave height H can be derived from the wave envelope as $H=2A$ (Ochi, 2005; Goda, 2010). For those wave fields that cannot be described as Gaussian and narrow-banded processes, the wave profile presents two or more local maxima and minima for one single wave cycle. In those cases a unique wave envelope cannot be defined properly (Ochi, 2005), and the wave height cannot be regarded as twice the envelope. Then it may be more appropriate to consider two statistically independent envelopes separated by one-half of the average wavelength. The Gaussian and narrow-band approach is used in further sections of this paper to estimate three-dimensional wave groupiness parameters from the wave envelope.

3. Wave grouping detection from the local and instantaneous envelope

Taking into account that the wave height H can be regarded as twice the wave envelope for Gaussian and narrow-banded wave fields (see the above Section (2.3)), a method to analyze wave groupiness features is to generalize the concept of run used in one dimension (e.g. wave elevation time series) (Medina and Hudspeth, 1990; Goda, 2010) to three dimensions (x,y,t). In one dimension a run length is defined as the number of consecutive waves with wave heights higher than a given threshold height H_0 (Goda, 2010). Hence, in the spatial domain (x,y) a run area can be defined by the region of the sea surface where the contiguous waves are higher than a given threshold height H_0 (Nieto-Borge et al., 2004a). Time dependence is included considering the temporal evolution of those run areas. Thus, the areas of each detected run, as well as the spatial distribution of them, and their respective temporal evolution in the oceanic area of study, provide information about the three-dimensional wave groupiness features of the sea state.

Wave grouping analysis considers consecutive waves of high waves of comparable heights. Therefore, the detection of the groupiness phenomenon must take into account different analysis than the study of extreme individual wave events, like rogue waves (Onorato et al., 2010; Gramstad and Trulsen, 2010, 2011), sharp crests (Baxevani and Richlik, 2004; Forristall, 2006; Fedele et al., 2011a, 2012), etc., which should not be considered as a group. In addition, it is well known that the estimation of the envelope by the HT, or any other multidimensional generalization, like RT, induces some additional components of high frequency (King, 2009a,b). These effects were taken into account in Longuet-Higgins (1984, 1986) by applying a band-pass filter to the wave elevation time series. Hence, a smoothed instantaneous envelope derived from the filtered wave elevation time series was estimated to carry out the wave group study in the one-dimensional case (e.g. the temporal domain). For wave grouping analysis in three dimensions (x,y,t), the wave envelope has to contain only long wave lengths and periods (low wave numbers and frequencies) defined by the second-order difference of wave number $(\mathbf{k}_m - \mathbf{k}_n)$ and frequency $(\omega_m - \omega_n)$ components of the relevant spectral components of the wave field $\eta(\mathbf{r}, t)$. For that purpose, in this work a three-dimensional low-pass filter in the $(\mathbf{k}, \omega)$-domain is applied to the envelope estimation derived from the RT given by Eq. (29). Hence, the short spatial and fast temporal contributions to the wave envelope are vanished. In this work the low-pass filter keeps all the spectral components of $A_r(\mathbf{r}, t)$ (e.g. the RT estimation of the envelope $A(\mathbf{r}, t)$) located for those wave numbers $\mathbf{k}_A$ and frequencies ω_A that hold the conditions $|\mathbf{k}_A| \leqslant 1.5|\mathbf{k}_p|$, and $\omega_A \leqslant 1.5\omega_p$, where $|\mathbf{k}_p|$ is the peak wave number derived from the directional spectrum $F(\mathbf{k})$ and ω_p is the peak frequency obtained from the scalar spectrum $S(\omega)$. The subindex A in $\mathbf{k}_A$ and ω_A indicates that those wave numbers and frequencies are related to the spectral components of the envelope rather the spectral components of the wave elevation field $\eta(\mathbf{r}, t)$. Hence, the vectors $\mathbf{k}_A$ are related to the wave number differences $(\mathbf{k}_m - \mathbf{k}_n)$ of $\eta(\mathbf{r}, t)$. In a similar way, the frequencies ω_A depend on the difference of the wave field frequencies $(\omega_m - \omega_n)$. Once the smoothed local and instantaneous envelope $\tilde{A}(\mathbf{r}, t)$ is obtained, and considering the wave field as a Gaussian narrow-banded process (see Section 2.3), the next step is to estimate the local and instantaneous wave height as $2\tilde{A}(\mathbf{r}, t)$. Hence, using the significant wave height as threshold height $H_0 = H_s$, the areas of the sea surface where consecutive waves higher than H_s can be analyzed. Extending the ideas used for wave elevation time series, those areas are called in this work as run areas. Applying this technique to consecutive time steps, the temporal evolution or the run areas can be investigated as well. Furthermore, to avoid the effect of some spikes that can remain in the smoothed envelope $\tilde{A}(\mathbf{r}, t)$, only significant run areas are taken into account. For that purpose, the mean wave size is computed from the wave number spectrum $F(\mathbf{k})$ using the so-called covariance matrix Λ (Krogstad et al., 2004)

$$\Lambda_{ij} = \int_{\mathbf{k}} k_i k_j F(\mathbf{k}) dk_x dk_y, \quad i, j = 1, 2; \tag{35}$$

where, following the notation used above, $k_1 \equiv k_x$, and $k_2 \equiv k_x$. The matrix Λ takes the form

$$\Lambda = \begin{pmatrix} \overline{k_x^2} & \overline{k_x k_y} \\ \overline{k_x k_y} & \overline{k_y^2} \end{pmatrix}. \tag{36}$$

The maximum and minimum eigenvalues of Λ (k_{max}^2 and k_{min}^2) are related with the mean wave length as $\lambda_m = 2\pi/\sqrt{k_{max}^2}$ and the mean crest length $\lambda_{wc} = 2\pi/\sqrt{k_{min}^2}$ respectively (Krogstad et al., 2004). Therefore, the mean wave size area is given by $\Delta_{ws} = \lambda_m \lambda_{wc}$. In this work only the run areas larger or equal than twice the mean wave size, $2\Delta_{ws}$, are taken into account.

4. Wave field analysis by using X-band marine radars

X-band marine radars are the common radar systems mounted on maritime traffic control towers, as well as on off shore platforms, and on moving vessels. Those radar systems are incoherent real aperture radars, working with horizontal polarization at grazing incidence (Skolnik, 2008). Although, marine radars are designed for navigation purposes, these systems are suitable to be used as a microwave remote sensing tool for oceanographic purposes (Buckley et al., 1994; Robinson et al., 2000; Wyatt et al., 2003; Reichert and Lund, 2007). This capability is based on the well-known fact that signatures of the sea surface are visible in the near range of X-band marine radar images (Young et al., 1985; Ziemer et al., 2004). These signatures are known as *sea clutter*, which is an undesirable signal for navigation purposes. Sea clutter is caused by the backscatter of the transmitted electromagnetic waves from the short sea surface ripples in the range of half the electromagnetic wavelength (i.e. ~1.5 cm) (Alpers et al., 1981; Frasier and McIntosh, 1996). Longer waves like swell and wind sea become visible as they modulate the backscatter signal mainly via different modulation mechanisms, such as the hydrodynamic modulation of the ripples caused by the interaction with the longer waves, tilt modulation due to the changes of the effective incidence angle along the long wave slopes, and the partial shadowing of the sea surface by higher waves (Keller and Wright, 1975; Alpers and Hasselmann, 1982; Plant, 1990; Lee et al., 1995). Since standard X-band marine radar systems allow to scan the sea surface with high temporal and spatial resolution, they are able to monitor the sea surface in both time and space (Nieto-Borge et al., 1999; Reichert and Lund, 2007). Thus, the combination of the temporal and spatial wave information allows the determination of unambiguous directional wave spectra, as well as their related sea state parameters, such as significant wave height (Nieto-Borge et al., 2008), mean wave lengths and periods, wave propagation directions (Izquierdo et al., 2005; Reichert et al., 2005), etc. Detail descriptions of the methods used to analyze wave fields with standard marine radars can be found in Nieto-Borge et al. (1999); Ziemer et al. (2004); Reichert et al. (2005); Reichert and Lund (2007). The analysis of radar image time series permits to derive additional information, such as the two-dimensional sea surface current (Young et al., 1985; Nieto-Borge and Guedes-Soares, 2000; Senet et al., 2001). Fig. 1 shows an example of sea clutter image time series acquired by a X-band marine radar system located in the North Sea. In addition to those statistical and spectral parameters that describe sea states, information of the wave elevation field η can be as well estimated for each sea surface position $\mathbf{r} = (x, y)$ and for different times t. That technique, which was originally published in Nieto-Borge et al. (2004b), permits to derive information of individual waves and it is briefly described in the following section.

4.1. Estimation of wave elevation fields from sea clutter image time series

The method to estimate the wave elevation field $\eta(\mathbf{r}, t)$ from X-band marine radar data sets is based on the structure of the so-called three-dimensional image spectrum $\mathcal{I}(\mathbf{k}, \omega)$ (e.g. the spectral density of the sea clutter image time series). The details of this technique can be consulted in Nieto-Borge et al. (2004b); Hessner et al. (2006); Hessner and Reichert (2007). This technique is based on an inversion modeling method to obtain the wave spectrum $\mathcal{F}(\mathbf{k}, \omega)$ from the image spectrum $\mathcal{I}(\mathbf{k}, \omega)$ (Nieto-Borge et al., 1999; Nieto-Borge and Guedes-Soares, 2000; Ziemer et al., 2004). The aim of the inversion method consists of taking into account that ocean wind-generated waves are dispersive (Young et al., 1985). Under the frame of the linear gravity wave theory, the dispersion relation is given by

$$\omega = \sqrt{g|\mathbf{k}| \tanh(|\mathbf{k}|h)} + \mathbf{k} \cdot \mathbf{U}, \tag{37}$$

where $\mathbf{U} = (U_x, U_y)$ is the surface current of encounter (Young et al., 1985; Senet et al., 2001). The main spectral components of the image spectrum in the $(\mathbf{k}, \omega)$-domain can be summarized as

- Wave components within the dispersion relation shell that hold Eq. (37) (Young et al., 1985).
- Higher harmonics of the dispersion relation due to the shadowing modulation (Senet et al., 2001; Nieto-Borge et al., 2008).
- Subharmonic of the dispersion relation, which sometimes is mentioned in the literature as *group line* (Stevens et al., 1999).
- Background spectral noise caused by the roughness of the sea surface due to the local wind (Nieto-Borge et al., 2004b; Nieto-Borge et al., 2008).

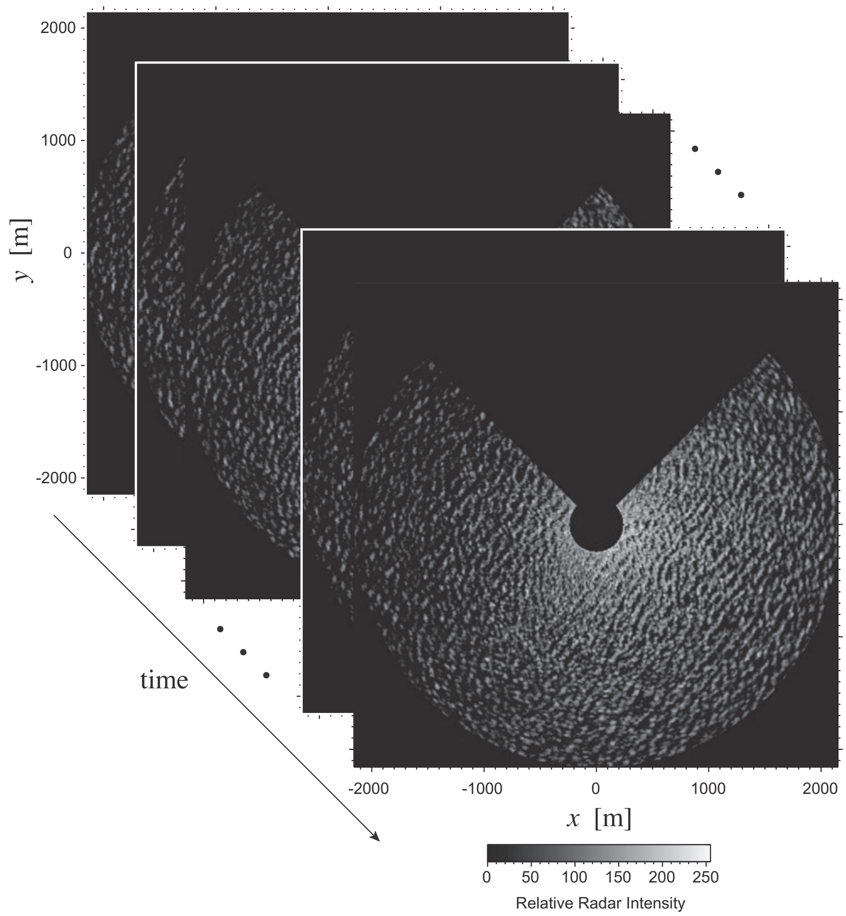

Fig. 1. Scheme showing an example of temporal sequence of sea clutter images measured by a X-band marine radar system located in the Southern North Sea. The black sector in the upper part of each sea clutter image corresponds to a blanked area in the direction of the platform where the radar is mounted.

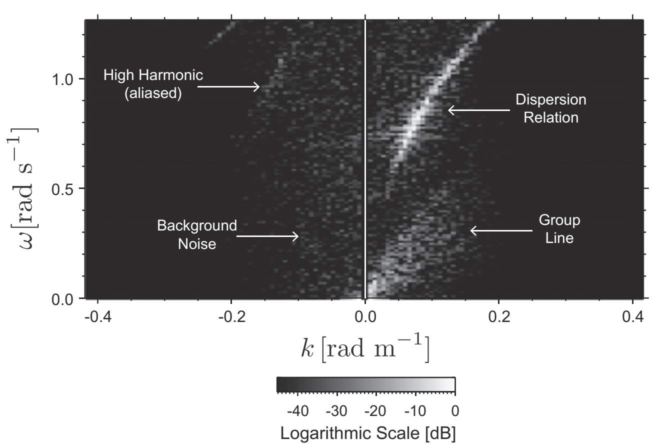

Fig. 2. Example of a image spectrum $\mathcal{I}$ indicating its main spectral contributions. The figure shows a two-dimensional transect along the mean wave propagation direction.

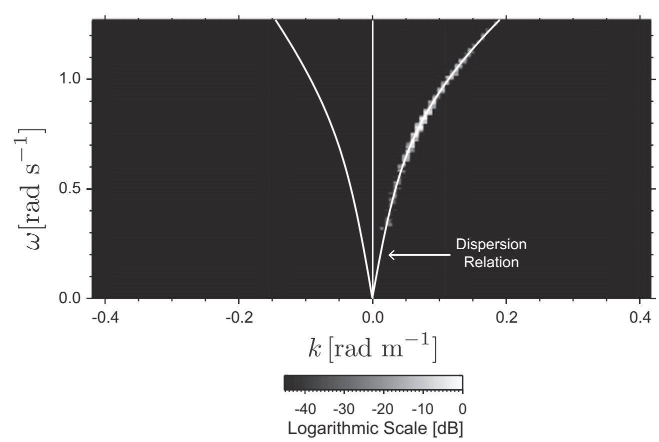

Fig. 3. Two-dimensional transect along the mean wave propagation direction of the estimation of the three-dimensional wave spectrum $\mathcal{F}$ derived from the image spectrum $\mathcal{I}$ shown in Fig. 2. It can be seen that only the spectral $(\mathbf{k}, \omega)$-components that hold the dispersion relation given by Eq. (37) are kept.

Fig. 2 shows an example of image spectrum $\mathcal{I}(\mathbf{k}, \omega)$ where some of the spectral components mentioned above can be identified. The estimation of the wave spectrum $\mathcal{F}(\mathbf{k}, \omega)$ is obtained by applying a three-dimensional band-pass filter in the $(\mathbf{k}, \omega)$-domain that suppresses those spectral components that do not hold the dispersion relation given by Eq. (37) (Nieto-Borge et al., 1999). To define this three-dimensional band-pass filter it is necessary to estimate previously the surface current of encounter $\mathbf{U}$ analyzing the distribution of the most energetic spectral components of the image spectrum (Young et al., 1985). Once, the three-dimensional band-pass filter is applied, an additional transfer function that correct the effect of the tilt modulation is used to obtain the estimation of $\mathcal{F}(\mathbf{k}, \omega)$ (Seemann et al., 1997; Nieto-Borge and Guedes-Soares, 2000). Fig. 3 illustrates the wave spectrum obtained from the im-

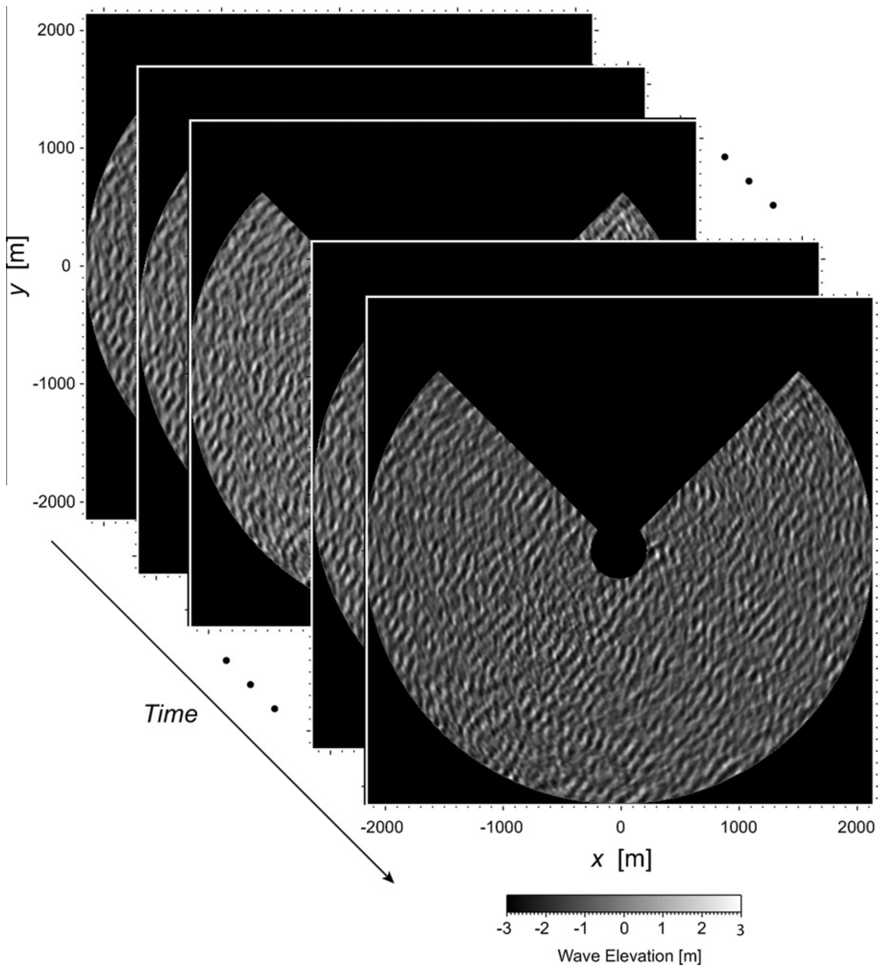

Fig. 4. Estimated wave elevation field derived from the sea clutter time series shown in Fig. 1.

age spectrum shown in Fig. 2 by applying this inversion modeling technique.

From the spectral density $\mathcal{F}(\mathbf{k},\omega)$, other spectral functions of the wave field can be derived as well, such as the two-dimensional wave number spectrum $F(\mathbf{k})$, the directional spectrum $E(\omega,\theta)$, and the scalar frequency spectrum $S(\omega)$ (Nieto-Borge and Guedes-Soares, 2000). In addition, taking into account that, for grazing incidence and horizontal polarization, which is the case of the marine radar, the main modulation mechanism is shadowing (Seemann, 1997; Nieto-Borge et al., 2004b), the water surface elevation η can be reconstructed for each sea surface position $\mathbf{r}=(x,y)$ and time t as

$$\eta(\mathbf{r},t)=\sum_{\mathbf{k}}\sum_{\omega}a_{\mathbf{k},\omega}\cos\left(\mathbf{k}\cdot\mathbf{r}-\omega t+\varphi_{\mathbf{k},\omega}\right) \tag{38}$$

where the amplitudes $a_{\mathbf{k},\omega}$ are derived from the estimation of the three-dimensional wave spectrum $\mathcal{F}(\mathbf{k},\omega)$, and the phases $\varphi_{\mathbf{k},\omega}$ are mainly induced by the shadowing and the strong backscatter of the wave crests (Nieto-Borge et al., 2004b, 2010). It is important to mention that, for marine radar conditions, although Eq. (38) is based on the assumption that shadowing is the dominant modulation mechanism, some authors consider that the role of the wave tilt is more important, even for grazing incidence (Plant and Farquharson, 2012). This fact is taken into account to retrieve the sea surface from temporal sequences of marine radar images (Dankert and Rosenthal, 2004). That method is an alternative approach to the technique used in this paper given by Nieto-Borge et al. (2004b).

Fig. 4 illustrates an example of the estimation of the sea surface derived from the time series of sea clutter images shown in Fig. 1 using Eq. (38). In practice, the sea clutter time series are sampled in space and time due to the spatial resolutions and the rotation period of the radar antenna. Therefore, the estimation of the wave elevation η given by Eq. (38) is sampled in the sea surface position $\mathbf{r}=(x,y)$ and time t as well. Furthermore, due to the method uses a three-dimensional DFT decomposition, the wave numbers $\mathbf{k}$ and frequencies ω take as well discrete values (Nieto-Borge and Guedes-Soares, 2000). Thus, the filter used in Eq. (38) consider a width along the dispersion relation shell given by Eq. (37). This width in the $(\mathbf{k},\omega)$-domain is related to the resolution in wave number $(\Delta k_x,\Delta k_y)$ and frequency $\Delta\omega$ (Young et al., 1985). The method to estimate the sea surface elevation given by Eq. (38) has been validated with some field experiments carried out in California using air-borne LIDAR and buoy data (Terrill and de, 2009). Once the sea surface elevation η is estimated for each position $\mathbf{r}=(x,y)$ and time t analysis of individual waves in the spatial and temporal domain can be carried out (Hessner et al., 2006; Hessner and Reichert, 2007). The comparison results carried out by Terrill and de (2009) indicate that, due to the range and azimuthal resolutions of the antenna, as well as due to the spatial scale where the shadowing effect occurs, the wave elevation fields estimated by the X-band radar describe properly the sea surface elevation for the $(\mathbf{k},\omega)$-domain where the spectral components $a_{\mathbf{k},\omega}$ present significant spectral energy. Hence, all the grouping properties derived from these data are related to the $(\mathbf{k},\omega)$-domain where the spectral energy is dominant.

5. Detection of wave groupiness from time series of sea clutter images

This section shows an example of the application of the theoretical assumptions described above to an estimation of wave elevation field $\eta(\mathbf{r}, t)$ retrieved from a measurement of sea clutter image time series acquired by a X-band radar station located in the North Sea.

5.1. Description of the measuring system

In this work, to measure and store the sea clutter radar data sets, an A/D converter (WaMoS-II) built up for the specific purpose of ocean wave monitoring has been used (Reichert et al., 2005; Reichert and Lund, 2007). WaMoS-II is an operational Wave Monitoring System originally developed at the German Research Institute Helmholtz–Zentrum Geesthacht (formerly known as GKSS Research Center). The measuring system consists of a conventional marine radar, a high-speed video digitizing and storage device and a standard computer (Reichert et al., 1999). The analog radar video signal is read out and digitized into range of grey levels. This information is transferred and stored on a computer where the wave analysis software carries out the computation of the sea state parameters in real time (Reichert et al., 2005). For WaMoS-II measurements, marine radar raw radar signals are analyzed. Hence, preprocessing radar filters (e.g. rain filter, anti clutter filter, image intensity amplification, etc.) are not used.

The data used in this work have been collected by the WaMoS-II station mounted at the German research platform of FINO 1, which belongs to the Federal Maritime and Hydrographic Agency of Germany (BSH). The platform is located in the German Bight in the Southern North Sea (54°01' N, 06°35' E), where the approximate water depth is 30 m. The radar controlled by the WaMoS-II system is a typical commercial marine radar (Furuno FR-2125-B) with a logarithmic amplifier and a peak power output of 25 kW operating at 9.5 GHz (X-band). The range resolution of the radar is 7.5 m. The antenna (type XN24AF/8) is 8-feet length (2.4 m), horizontally polarized with a horizontal beamwidth of 0.95°. The radar antenna rotates with a period of 2.5 s (24 rpm), which is the sampling time of the sea clutter time series. The antenna is mounted in the plat-

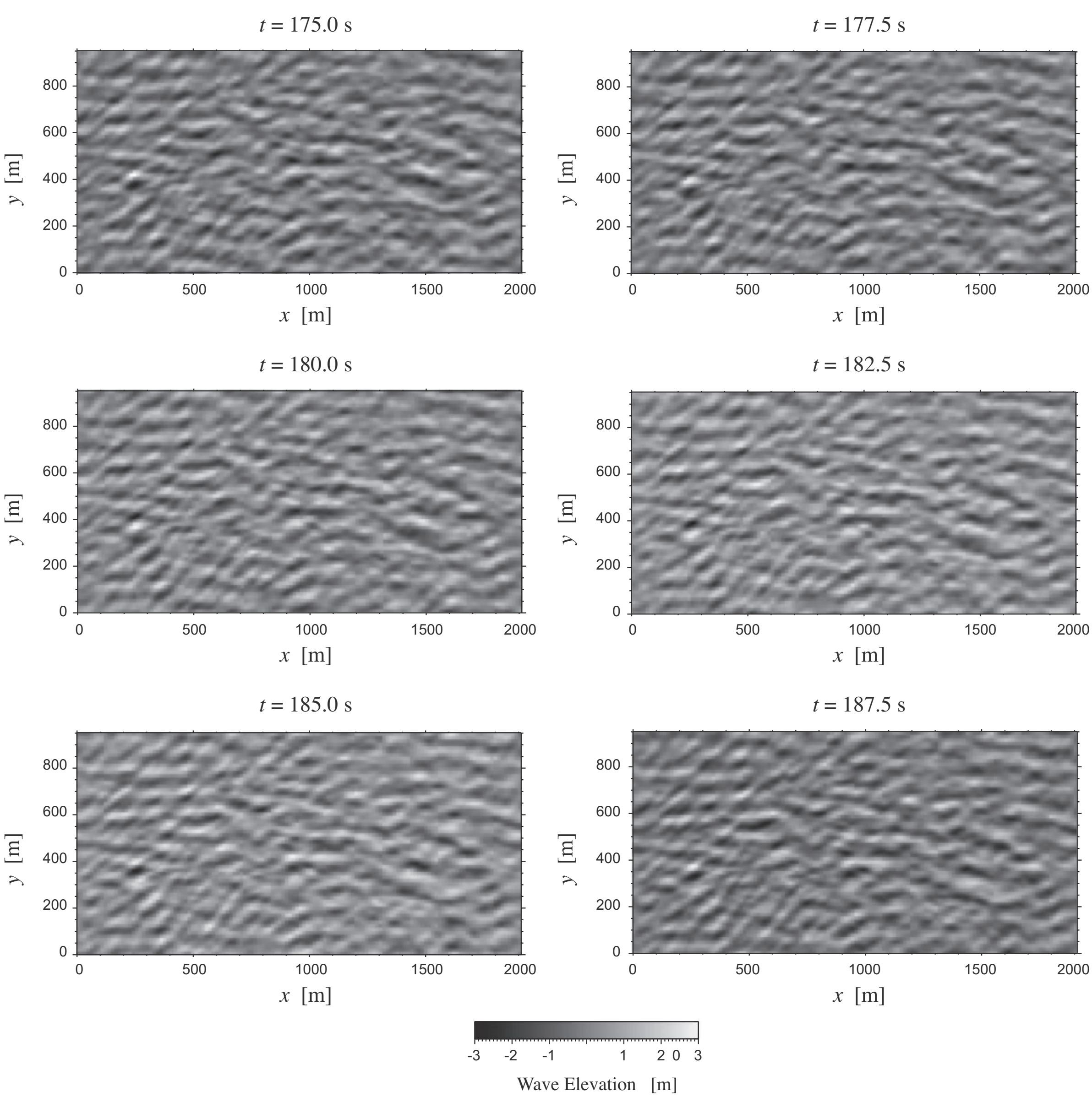

Fig. 5. Estimated wave elevation field derived from a sea clutter image for different time steps.

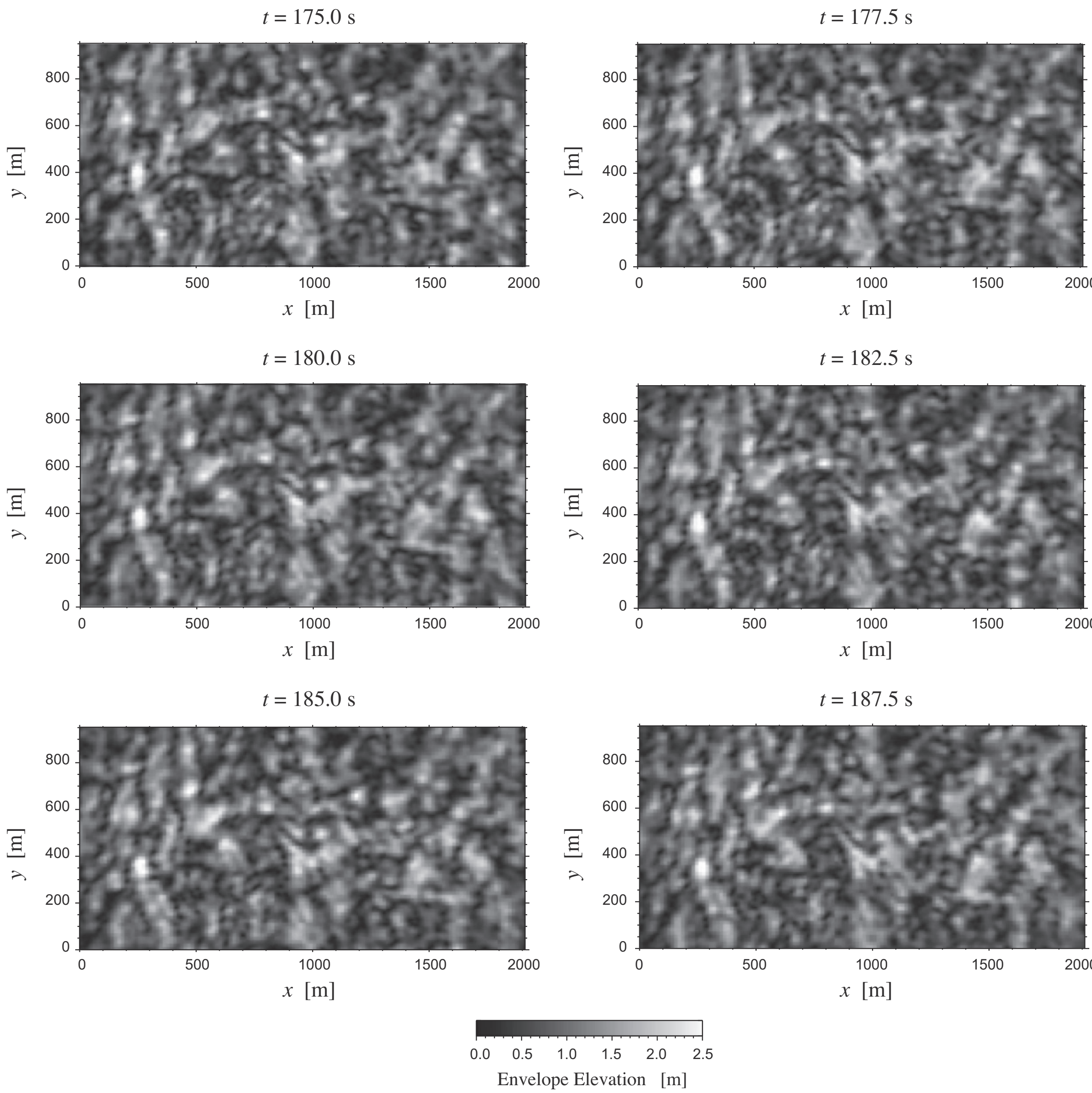

Fig. 6. Local and instantaneous wave envelope corresponding to the estimated wave elevation field shown in Fig. 5. The envelope has been computed from a Riesz Transform by using Eq. (29).

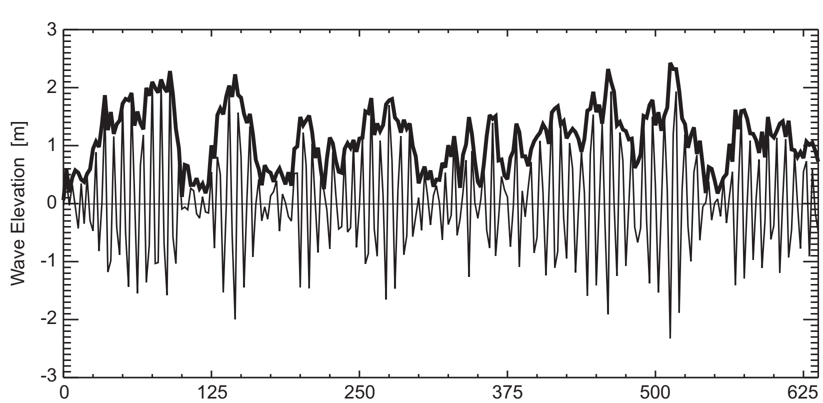

Fig. 7. Time series of the wave elevation evaluated at the central position of the sea surface area shown in Fig. 5 (thin line). The corresponding estimation of the temporal evolution of the two-dimensional wave envelope derived from the Riesz transform illustrated in Fig. 6 is as well represented (thick line).

form about 20 m over the means sea level. For the case of FINO 1, the WaMoS-II set up samples the sea clutter intensity values in a range of 256 gray levels (e.g. one unsigned byte). The maximum sampled range of the radar images is set up to 2 km from the platform. For operational purposes, the WaMoS-II installed at FINO 1 provides in routine the directional spectra, as well as the derived sea state parameters. For that operational use, the WaMoS-II system at FINO 1 measures temporal sequences composed of 32 consecutive sea clutter images to extract sea state parameters in near real time. The time coverage of the sea clutter time series used for operational purposes (e.g. $32 \times 2.5 = 80$ s) is enough for spectral estimation but not for wave grouping analysis because the envelope evolves in time slower than the individual waves. For that reason, longer time series has been measured changing the set-up of the WaMoS-II configuration. The results shown in this section correspond to a WaMoS-II measurement of a time series composed of 256 consecutive sea clutter images (e.g. total time coverage of the time series equal to $256 \times 2.5 = 640$ s).

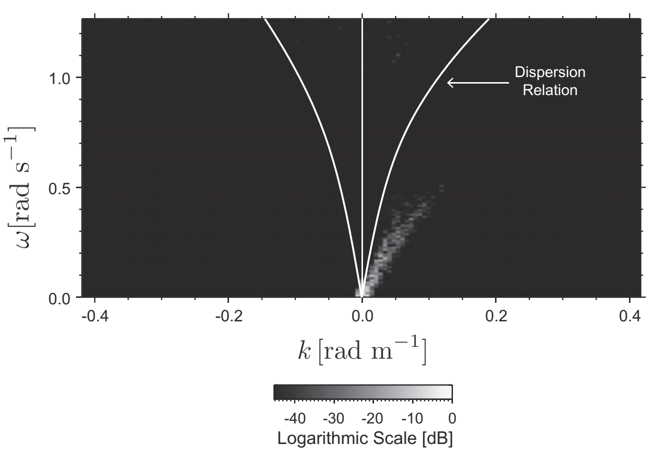

Fig. 8. Two-dimensional transect along the mean propagation direction of the three-dimensional spectral density of the local and instantaneous envelope. The white line indicates the dispersions relation of the wave field shown in the spectrum of the Fig. 3.

5.2. Experimental results

This sections shows the results of the wave grouping feature detection from a time series of sea clutter images. The data were taken on November 11, 2008 at the FINO 1 platform at 5:00 pm. The measurement corresponds to the previously shown sea clutter images and the associated inverted wave field shown in Figs. 1, and 4 respectively. Form the standard X-band marine radar analysis based on the estimation of the wave spectrum, the measured sea state had a significant wave height of $H_s = 3$ m, with a mean wave length $\lambda_m = 95.4$ m, peak wave length $\lambda_p = 105.4$ m, mean wave period $T_m = 7.9$ s, and peak period $T_p = 8.2$ s. Using the method proposed by Senet et al. (2001), the fit of the surface current of encounter gave a value for the current speed of 0.5 m s^{-1}, with a directional shift from the mean wave propagation direction of $+3.2^\circ$. The results of the different analyses shown in this section have been carried out for an area of approximately 2×1 km^2, where the radar shadowing modulation is dominant to retrieve a reliable estimation of the wave field (Terrill and de, 2009). Fig. 5 shows the estimated wave elevation field for the area of study and for different time steps in the measuring sequence of 256×2.5 s $= 640$ s. The corresponding local and instantaneous envelope estimation from RT given by Eq. (29) is shown in Fig. 6. Time series of this envelope evaluated at the central location of the sea surface area shown in Fig. 6, as well as the estimated wave elevation field, can be seen in Fig. 7. To illustrate how the spectral components of the local and instantaneous envelope are distributed in the $(\mathbf{k}, \omega)$-domain, Fig. 8 shows the spectral density of the envelope $A(\mathbf{r}, t)$. Comparing this figure with the wave spectrum shown in Fig. 3, it can be seen that the main energy of the spectral components of the envelope is located in low wave numbers and low frequencies (e.g. long scale of the spatio-temporal evolution), which is consistent with the fact of the spectral components of the local and instantaneous envelope $A(\mathbf{r}, t)$ can be explained by the differences of the dominant wave numbers and frequencies of the wave elevation field (see previous Section (2)). Due to this fact, the spectral components of the wave envelope are located in a smaller volume of the $(\mathbf{k}, \omega)$-domain than the spectral components of the corresponding wave elevation field. Integrating the three-dimensional spectra over all the domain of positive frequen-

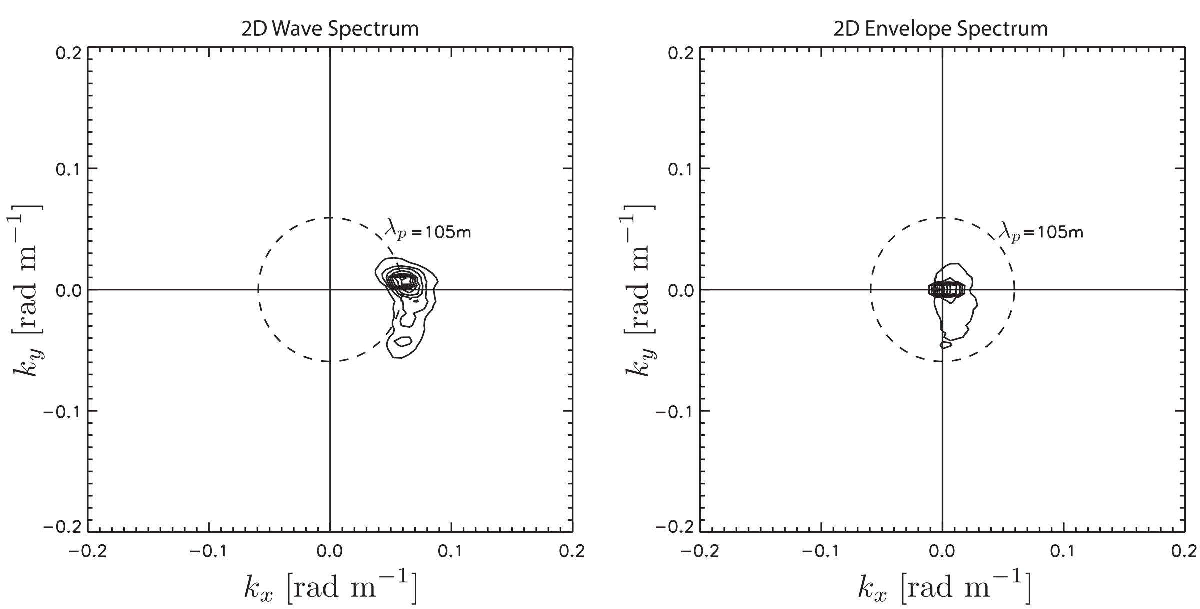

Fig. 9. Two-dimensional wave spectrum $F(\mathbf{k})$ (left) and the corresponding two-dimensional wave number spectrum of the local and instantaneous envelope (right) obtained by integrating their respective there-dimensional spectra over all the domain of positive frequencies $\omega > 0$.

cies $\omega > 0$, two-dimensional wave number spectral densities can be derived. Fig. 9 shows the two-dimensional wave spectrum $F(\mathbf{k})$ (left side of the figure) and the corresponding two-dimensional wave number spectrum of the local and instantaneous envelope (right side of the figure). It can be seen that the energy of the envelope spectrum is mainly located in the region of very low wave numbers (e.g. close to the origin of the (k_x, k_y)-domain). Furthermore, there is no relevant energy of the envelope of spatial scales lower than the peak wave length λ_p (wave numbers greater than $2\pi/\lambda_p$). In addition to the two-dimensional wave spectra, the frequency spectra of the envelope can be as well estimated by integrating the three-dimensional spectrum over all the domain of wave numbers. Fig. 10 shows the one-dimensional frequency spectra of the wave field and the envelope. In a similar way than the case of the two-dimensional wave number spectra, the most significant distribution of the spectral components of the envelope are located at frequencies lower than the peak frequency f_p of the wave field. It can be seen that some small energy appears for higher frequencies greater than f_p. Like in the one-dimensional case with the use of the Hilbert Transform (King, 2009a), these high frequency components correspond to the short term evolution that appear in the estimation of the wave envelope by the Riesz Transform. Taking into account these results, it is justified to apply a low-pass filter to the local and instantaneous envelope to suppress all the energy of the spectral components with wave numbers greater than the peak wave number $k_p = |\mathbf{k}_p|$ and the peak frequency $\omega_p = 2\pi f_p$. Fig. 11 shows the smoothed envelope by suppressing all the energy of the spectral components with wave numbers and frequencies larger than (k_p, ω_p). Once, the smoothed local and instantaneous envelope $\tilde{A}(\mathbf{r}, t)$ is estimated, and taking into account that the wave height can be regarded local and instantaneously as twice the amplitude, the run areas for different time steps can be obtained. Hence, using the significant wave height as the threshold height, $H_0 = H_s$, those oceanic areas where consecutive propagating waves higher than H_s can be analyzed. Fig. 12 shows the corresponding run areas computed from the smoothed envelope shown in Fig. 11. Note that, for this particular case, and due to the relation between the measured wave lengths and the water depth, the measurement corresponds to intermediate water depth conditions. Therefore, for this case, the assumption that the wave height is regarded as twice the amplitude can be consider like a first order approach.

Fig. 13 shows the temporal evolution of the local and instantaneous envelope $A(\mathbf{r}, t)$ along a sea surface transect parallel to the mean wave propagation direction. Two estimations of the envelope appear in Fig. 13: the raw envelope, as it is computed from the RT, $A_r(\mathbf{r}, t)$ (see Eq. (29)), and the corresponding smoothed envelope $\tilde{A}(\mathbf{r}, t)$ obtained after the low-pass filtering technique previously mentioned. In addition, Fig. 13 indicates the group velocities for three wave number values: $\mathbf{k}_c/2, \mathbf{k}_c$, and $3\mathbf{k}_c/2$, where, likely in the figures shown above, the characteristic wave number $\mathbf{k}_c$ is considered as the mean wave number derived from the covariance matrix defined in Eq. (35). It can be seen that the temporal evolution of both estimations of the envelope propagate with speeds close to the group velocity of the mean wave number (e.g. the group velocity of the mean wave length). That means that, although the wave field has a significant directional spreading (see the wave number spectrum $F(\mathbf{k})$ shown on the left of Fig. 9), there is no a high spread on the propagation speed of the local and instantaneous wave envelope.

Fig. 14 shows the temporal evolution along a sea surface transect parallel to the mean wave propagation direction of the local

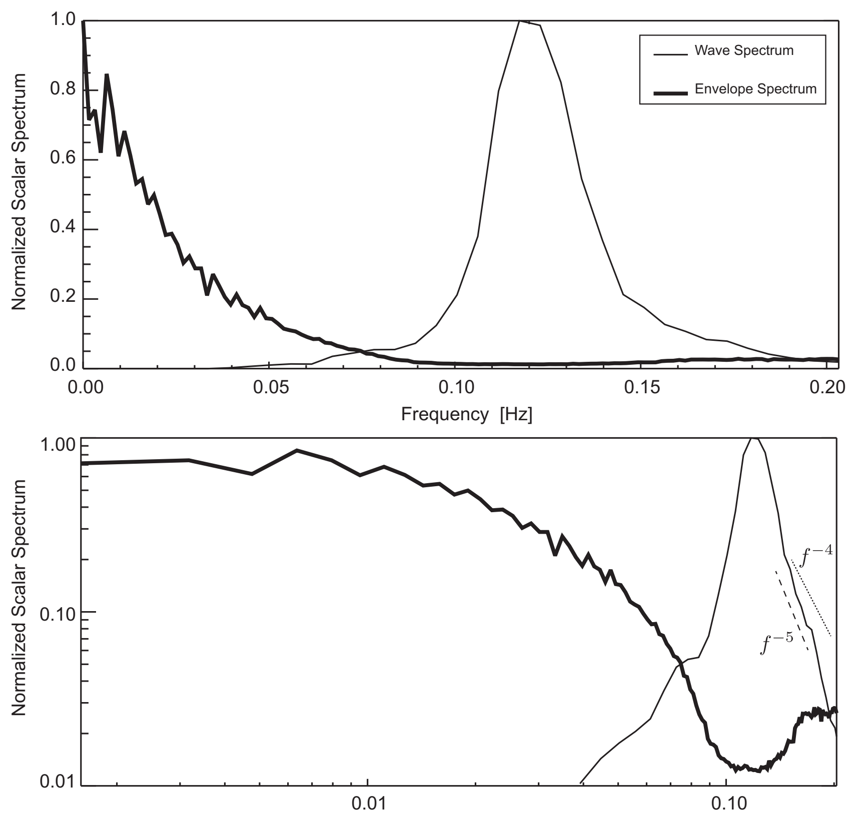

Fig. 10. One-dimensional frequency spectrum of the wave field (thin line) and the envelope (thick line) obtained by integrating their respective three-dimensional spectra over all the wave number domain. Both spectra have been normalized to their respective maximum values. The upper and the lower plots represent the spectra in linear and logarithmic scale respectively. In addition, the lower plot indicates the high frequency power decay dependence for f^{-4} and f^{-5}.

and instantaneous potential energy per unit of area $E_p(\mathbf{r},t)$, given by Eq. (3), and the local and instantaneous kinetic energy per unit of area $E_k(\mathbf{r},t)$, given by Eq. (11), where the parameter h in the integral of Eq. (11) has been taken as the mean water depth in the area of FINO 1 ($h = 30$ m). It can be seen in Fig. 14 that, although both local and instantaneous energies per unit of area present a short scale variability in space and time, as a result of being a local and instantaneous energetic features of the wave field, their large scale of the spatio-temporal evolution is close to the group velocity of the mean wave number, what suggests that most relevant wave length to describe the evolution of the energy and groupiness features is the mean wave length λ_m.

The temporal evolution of the run areas along the mean wave direction can be seen in top left of Fig. 15. This figure shows that the run areas if consecutive waves higher than H_s have a averaged size of $\approx 5\lambda_m$. That indicates that, in this measurement, the grouping phenomenon causes the formation of groups of waves higher than H_s composed on average of 5 consecutive waves. These groups appear and disappear as a result of the spatio-temporal evolution of the envelope. In addition, Fig. 15 shows the temporal evolution of the run areas along different propagation directions. It can be seen that the coherence of the runs decrease as the orientation of the transect of the sea surface keeps away from the mean wave direction θ_m. That result suggests that the local and instantaneous envelope and the wave energy propagate mainly close to θ_m. Some theoretical results concerning this fact were addressed in previous theoretical works, such as (Yefimov and Babanin, 1991).

The analysis carried out in this section is based on the structure and behavior of the local and instantaneous envelope $A(\mathbf{r},t)$. The following section compares the techniques described previously with standard wave groupiness information derived from the temporal domain. These comparisons, have been achieved by using simulated wave fields considering a stochastic approach.

6. Comparison of the spatio-temporal groupiness analysis with temporal information using simulated sea surfaces

The results shown in the previous section were derived from the spatio-temporal analysis of the envelope $A(\mathbf{r},t)$. These results have to be consistent with the wave grouping standard parameters

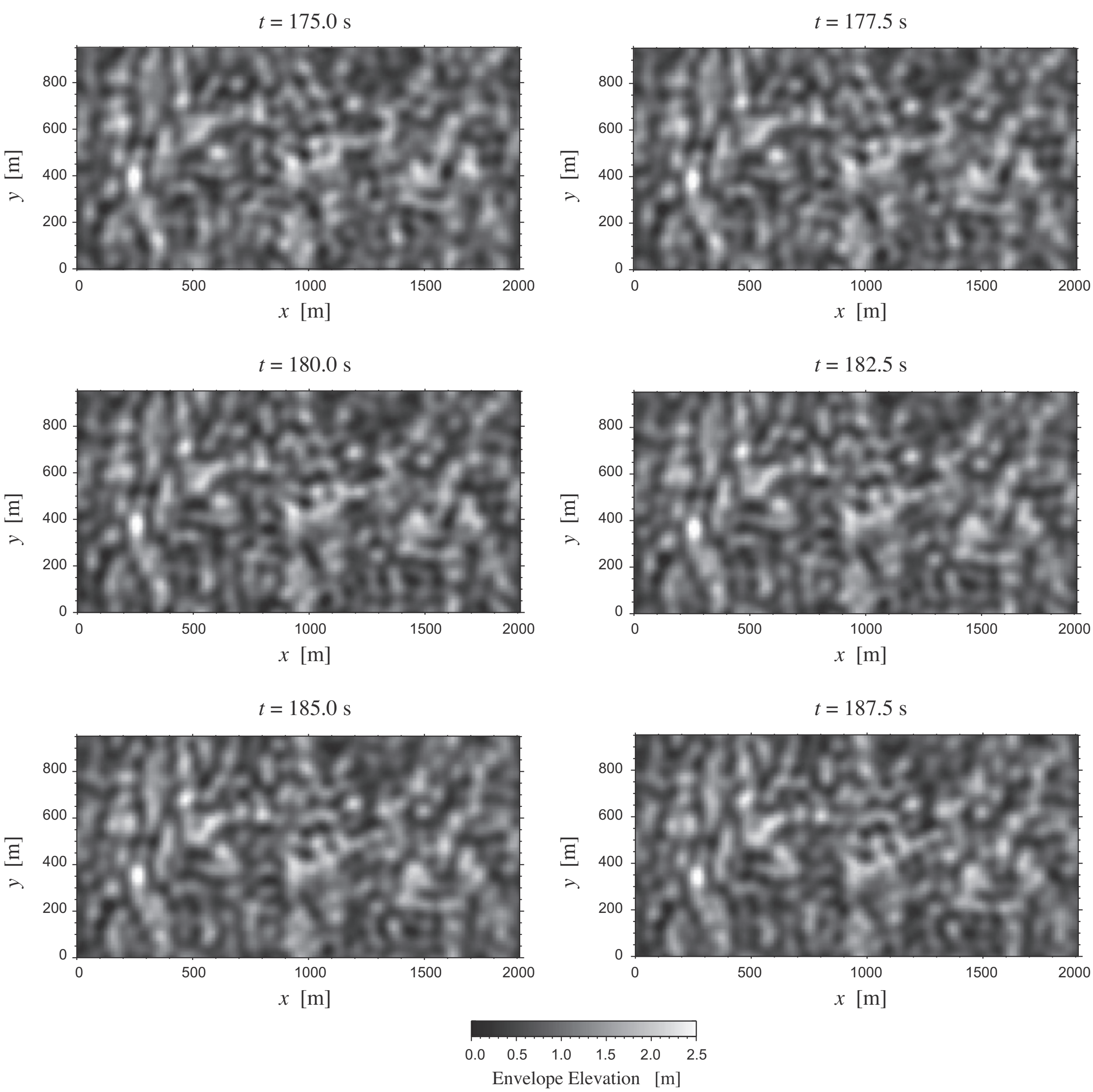

Fig. 11. Smoothed local and instantaneous envelope $\tilde{A}(\mathbf{r},t)$ for different time steps. The data have been obtained by applying a low-pass filter to the envelope estimated by the Riesz Transform shown in Fig. 6.

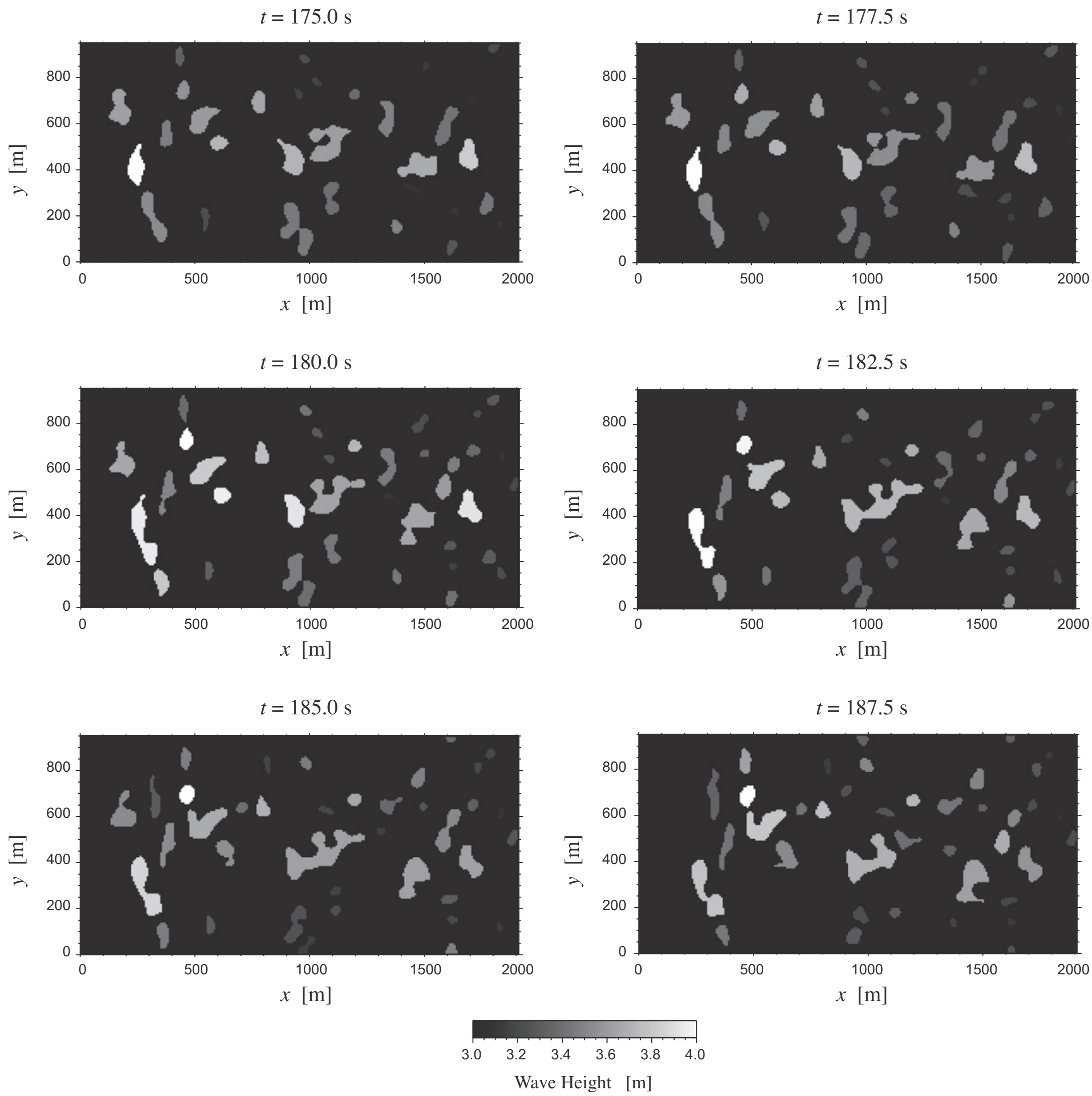

Fig. 12. Estimation of the run areas for different time steps derived from the smoothed local and instantaneous envelope $\tilde{A}(\mathbf{r}, t)$ shown in Fig. 11. The threshold height used to define the run areas is the significant wave height H_s. The areas are color coded using the mean wave height within each run area.

used for wave elevation time series. One of those parameters is the temporal correlation of consecutive have heights γ (Kimura, 1980; Longuet-Higgins, 1984). The parameter γ depends on the mean period T_m derived from the frequency spectrum $S(f)$.

To compare the spatio-temporal analysis used for the local and instantaneous envelope $A(\mathbf{r}, t)$ with γ, different simulated wave elevation fields $\eta(\mathbf{r}, t)$ have been carried out. Each simulation considers a theoretical parameterization of the wave spectrum. The spectrum $F(\mathbf{k})$ used for each simulated sea state is obtained form a JONSWAP spectrum and a directional spreading function using the parameterization given by Mitsuyasu et al. (1980). Therefore, the simulated sea surfaces correspond to wind sea cases. The achieved simulations cover a range of peak frequencies f_p between 0.1 Hz and 0.15 Hz, and significant wave heights H_s between 3 m and 10 m. The simulated sea surfaces cover an area similar to the area scanned by the X-band radar in FINO 1, with the same length of the temporal sequence (e.g. 256 time steps), and the same spatial and temporal resolutions ($\Delta x = \Delta y = 7.5$ m, and $\Delta t = 2.5$ s).

Under the frame of the linear wave theory, the simulation of the sea surface $\eta(\mathbf{r}, t)$ takes into account the stochastic model given by Eq. (1). Considering the dispersion relation $\omega(\mathbf{k})$ (see Eq. (37)) the sea surface for a given time t can be expressed in terms of two-dimensional DFT. In that case, the wave number vectors are discretized $(\Delta k_x, \Delta k_y)$. This linear wave model assumes the phases $\varphi_{\mathbf{k}}$ as uniform-distributed random variables in the interval $[-\pi, \pi)$, and the amplitudes $a_{\mathbf{k}}$ are Rayleigh-distributed. These random amplitudes $a_{\mathbf{k}}$ depend on the wave number spectrum $F(\mathbf{k})$ as $a_{\mathbf{k}} = \sqrt{F(\mathbf{k})\Delta k_x \Delta k_y/2} \cdot (\alpha_{\mathbf{k}}^2 + \beta_{\mathbf{k}}^2)^{1/2}$, being $\alpha_{\mathbf{k}}$ and $\beta_{\mathbf{k}}$ zero-mean and unit-variance Gaussian random variables. For each sea state conditions different realizations have been carried out to simulate the statistical variability of wave fields.

Fig. 16 shows the scatter plots of the mean run areas (e.g. spatio-temporal analysis) versus the temporal correlation of consecutive wave heights γ derived from the JONSWAP spectrum. The scatter plots are grouped depending on the peak frequency

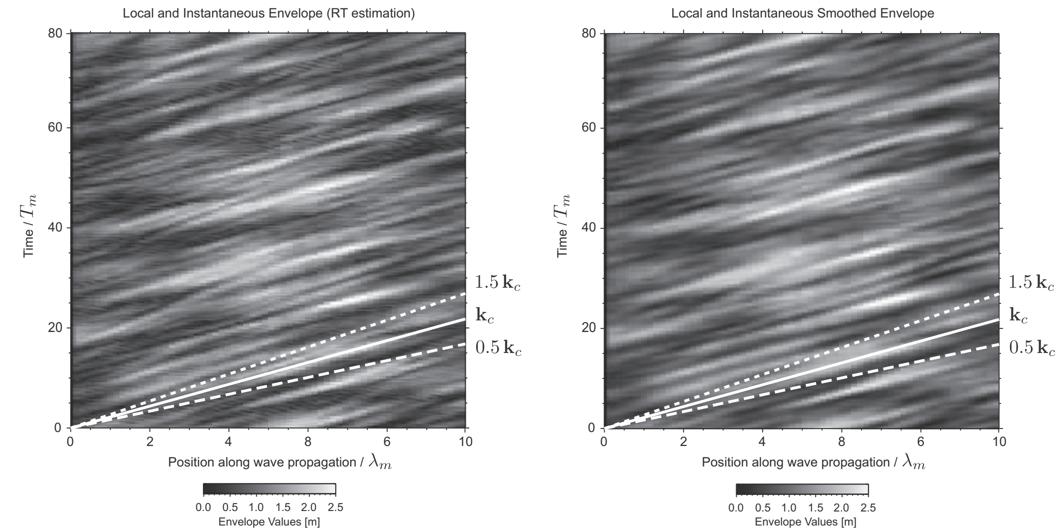

Fig. 13. Temporal evolution of the local and instantaneous envelope $A(\mathbf{r},t)$ along a transect of the sea surface parallel to the mean wave propagation direction. Two envelope estimation are shown in the figure: the estimation derived from the RT, $A_r(\mathbf{r},t)$ (left), and the corresponding smoothed envelope, $\tilde{A}(\mathbf{r},t)$, resulting of the application of a low-pass filter (right). The white straight lines correspond to the group velocities for different values of the wave number, which are, from the faster to the slower group velocity: $0.5\mathbf{k}_c, \mathbf{k}_c$, and $1.5\mathbf{k}_c$.

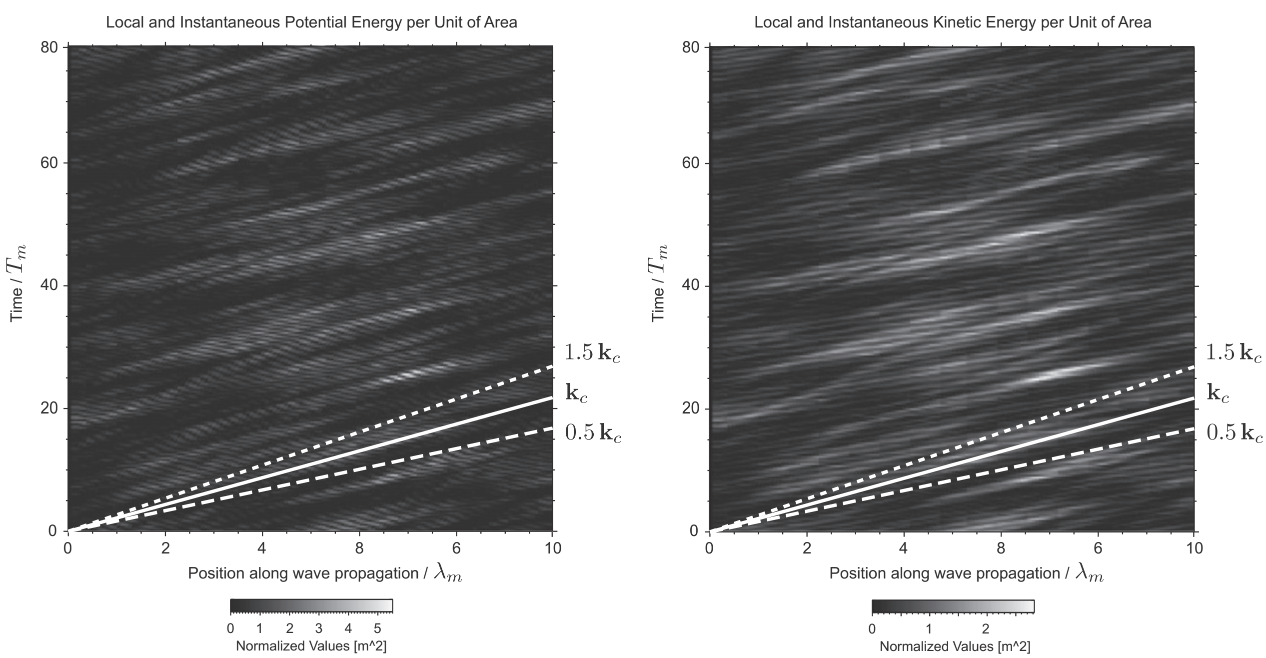

Fig. 14. Temporal evolution along a sea surface transect parallel to the mean wave propagation direction of the local and instantaneous potential energy per unit of area $E_p(\mathbf{r},t)$ (left), and the local and instantaneous kinetic energy per unit of area $E_k(\mathbf{r},t)$ (right). The data are normalized by dividing by the water density and the acceleration of gravity, ρg.

f_p used in each parameterization of the JONSWAP spectrum. It is known that the groupiness effect is more intensive when γ increases. Fig. 16 illustrates how γ increases as the mean run area of the simulated wave field increases as well. Furthermore, it can be seen that mean run areas grow as f_p decreases. This effect is due to the lower frequencies imply larger wave lengths, which lead to obtain larger run areas of consecutive waves. Hence, the results shown in Fig. 16 indicate that the spatio-temporal analysis proposed in the previous sections provide consistent results with the temporal domain analysis of wave groups.

7. Conclusions and outlook

This work analyses wave groupiness features in the spatio-temporal domain by using temporal sequences of sea clutter images acquired by common X-band marine radars. The analysis is based on the study of the behavior of the local and instantaneous envelope derived from a Gaussian narrow-banded wave field. The estimation of the envelope is carried out from the Riesz Transform applied to times series of wave elevation areas of the sea surface derived from the X-band radar. The obtained results indicate that the local instantaneous wave envelope, as well as other related

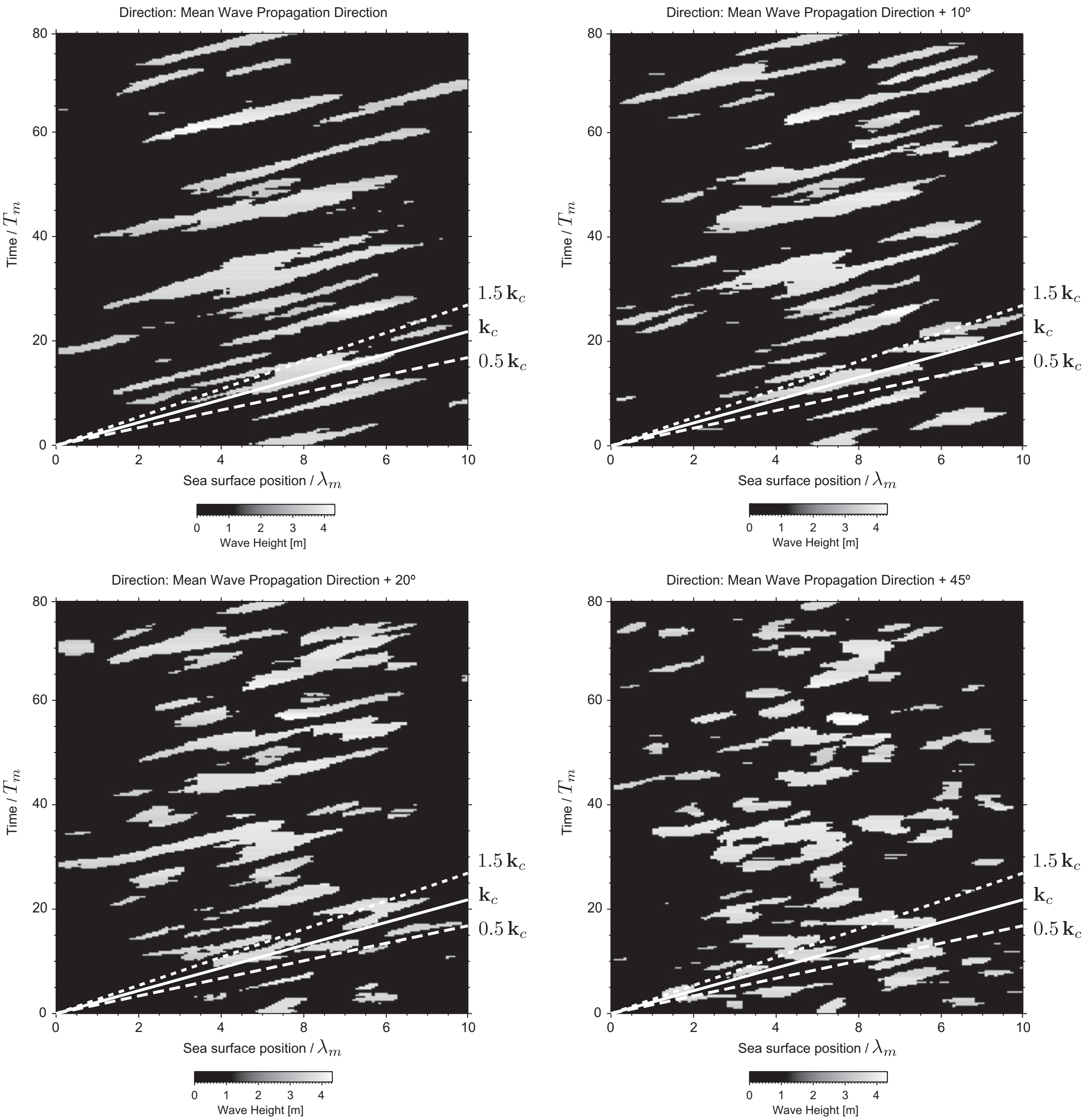

Fig. 15. Temporal evolution of the run areas for different directions: mean wave propagation direction θ_m (top left), $\theta_m + 10^\circ$ (top right), $\theta_m + 20^\circ$ (bottom left), $\theta_m + 45^\circ$ (bottom right).

magnitudes, such as the local and instantaneous energy per unit of area, propagate mainly with the group velocity of the mean wave length, which indicates that there is no a high spreading in the propagation velocities of the groups and the wave energy. In addition, as a further analysis of the wave grouping, the concept of run, which is used to the analysis of wave groups in one dimension, has been generalized to the spatio-temporal domain. Hence, defining a threshold height, set in this work to significant wave height, it is possible to determine the temporal evolution of the areas of the sea surface where consecutive high waves propagate in the ocean. The analysis of those run areas permits to study the stability of the groups as well as their extension and duration in terms of the mean wave length and periods.

To compare the spatio-temporal analysis with standard one-dimensional wave grouping parameters, the mean run area of sea states were compared with the temporal correlation of consecutive wave heights. For that purpose, a set of stochastic simulations of wind sea states have been synthesized. The result of the simulations indicate that the mean run areas grow as the wave height correlation in time increases. This result indicates that the methods applied in this work for the characterization of wave groupiness in space and time are consistent with the standard analysis based on the one-dimensional study of wave elevation time series.

Although the methods used in this work have been applied to the estimated water surface elevation fields derived from time series of sea clutter images, these techniques can be as well applied to any other sensor, or array of sensors, capable of measuring temporal sequences of wave elevation for larger areas of the ocean. These spatial temporal remote-sensing methods (e.g. X-band radars, video-based systems, etc.) would permit to carry out field experi-

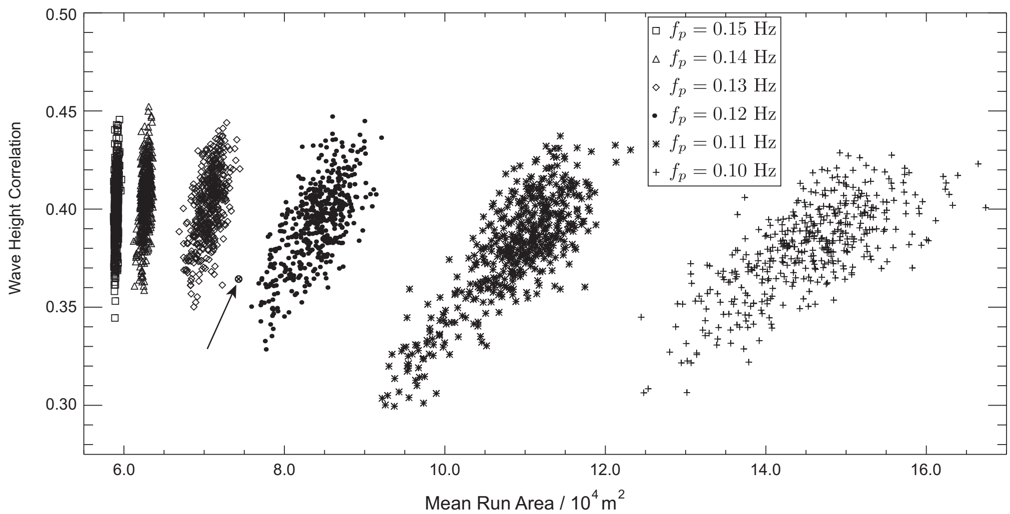

Fig. 16. Scatter plot of the mean run area depending on the temporal correlation of consecutive waves γ derived from stochastic simulated sea surfaces. The threshold height used to obtain the run areas is the significant wave height, $H_0 = H_s$. The arrow indicates the results obtained from the radar measurement used in paper (see Section (5.2)), where $\gamma = 0.364$, and the mean run area $= 74137.9$ m^2, being $f_p = 1/T_p = 0.122$ Hz.

ments, in combination with in situ sensors, to understand in more detail the spatio-temporal behavior of the wave grouping phenomenon.

Acknowledgements

This work has been supported by Ministerio de Ciencia e Innovación and Ministerio de Economía y Competitividad under project number TEC2009-14217. The WaMoS-II data obtained at the FINO 1 Platform were kindly provided by the Federal Maritime and Hydrographic Agency of Germany (Bundesamt für Seeschiffahrt und Hydrographie, BSH).

References

Alpers, W., Hasselmann, K., 1982. Spectral signal to clutter and thermal noise properties of ocean wave imaging synthetic aperture radars. Int. J. Remote Sens. 3, 423–446.

Alpers, W., Ross, D.B., Rufenach, C., 1981. On the delectability of ocean surface waves by real and synthetic aperture radar. J. Geophys. Res. 86 (C7), 6481–6498.

Baxevani, A., Richlik, I., 2004. Maxima for Gaussian seas. Ocean Eng. 33 (7), 895–911.

Bell, P.S., Williams, J.J., Clark, S., Morris, B.D., Vila-Concejo, A., 2005. Nested radar systems for remote coastal observations. J. Coastal Res. 39, 483–487.

Benetazzo, A., Fedele, F., Gallego, G., Shih, P.C., Yezzi, A., 2012. Offshore stereo measurements of gravity waves. Coastal Eng. 64, 127–138.

Buckley, J.R., Aler, J., 1997. Estimation of ocean wave height from grazing incidence microwave scatter. In: IEEE International Symposium on Geoscience and Remote Sensing – IGARSS 1997, vol. 2, pp. 1015–1017.

Buckley, J.R., Aler, J., 1998. Enhancements in the determination of ocean surface wave height from grazing incidence microwave backscatter. In: IEEE International Symposium on Geoscience and Remote Sensing – IGARSS 1998, vol. 5, pp. 2487–2489.

Buckley, J.R., Allingham, M., Michaud, R., 1994. On the use of marine radar imagery for estimation of properties of the directional spectrum of the sea surface. Atmosphere–Ocean 32 (1), 195–213.

Bülow, T., Pallek, D., Sommer, G., 2000. Riesz transforms for the isotropic estimation of the local phase of moire interferograms. In: 22nd DAGM Symposium Mustererkennung, pp. 1–8.

Clauss, G.F., Kosleck, S., Testa, D., Hessner, K., 2008. Forecast of critical situation in short-crested seas. In: 27th International Conference on Offshore Mechanics and Arctic Engineering, OMAE 2008. ASME, pp. 1–10.

Dankert, H., Horstmann, J., Lehner, S., Rosenthal, W., 2003. Detection of wave groups in Sar images and radar image sequences. IEEE Trans. Geosci. Remote Sens. 41 (6), 1437–1446.

Dankert, H., Rosenthal, W., 2004. Ocean surface determination from X-band radar–image sequences. J. Geophys. Res. 109 (C4), 1–11.

Donelan, M.A., Drennan, W.M., Magnusson, A.K., 1996. Nonstationary analysis of the directional properties of propagating waves. J. Phys. Oceanogr. 26 (9), 1901–1914.

Fedele, F., 2012. Space-time extremes in short-crested storm seas. J. Phys. Oceanogr..

Fedele, F., Benetazzo, A., Forristall, G., 2011a. Space–time waves and spectra in the northern adriatic sea via a wave acquisition stereo system. In: 30th ASME International Conference Offshore Mechanics and Arctic Engineering, Rotterdam, The Netherlands, OMAE 2011-49924(6), pp. 651–663.

Fedele, F., Cherneva, Z., Tayfun, M.A., Guedes-Soares, C., 2011b. NLS invariants and nonlinear wave statistics. Phys. Fluids 22 (036601).

Fedele, F., Gallego, G., Benetazzo, A., Yezzi, A., Sclavo, M., Bastianini, M., Cavaleri, L., 2011c. Euler characteristics and maxima of oceanic sea states. J. Math. Comput. Simul. 82 (6), 1102–1111.

Forristall, G.Z., 2006. Maximum wave heights over an area and the air gap problem. In: 25th ASME International Conference on Offshore Mechanics and Arctic Engineering, Hamburg, Germany, OMAE 2006-92022, pp. 11–15.

Frasier, S.J., McIntosh, R.E., 1996. Observed wavenumber–frequency properties of microwave backscatter from the ocean surface at near-grazing angles. J. Geophys. Res. 101, 57–79.

Gallego, G., Yezzi, A., Fedele, F., Benetazzo, A., 2011. A variational stereo method for the three-dimensional reconstruction of ocean waves. IEEE Trans. Geosci. Remote Sens. 49 (11), 4445–4457.

Goda, Y., 2010. Random Seas and Design of Maritime Structures. World Scientific.

Gramstad, O., Trulsen, K., 2010. Can swell increase the number of freak waves in a wind sea? J. Fluid Mech. 650, 57–79.

Gramstad, O., Trulsen, K., 2011. Fourth-order coupled nonlinear Schrödinger equations for gravity waves on deep water. Phys. Fluids 23, 1–9.

Gran, S., 1992. A Course in Ocean Engineering. Elsevier Science Publishers.

Hamilton, J., Hui, W.H., Donelan, M.A., 1979. A statistical model for groupiness in wind waves. J. Geophys. Res. 84, 4875–4884.

Hessner, K., Reichert, K., 2007. Sea surface elevation maps obtained with a nautical X-band radar – examples from WaMoS II stations. In: 10th International Workshop on Wave Hindcasting and Forecasting and Coastal Hazard Symposium in North Shore, Oahu, Hawaii, USA, pp. 1–12.

Hessner, K., Reichert, K., Dannenberg, J., 2006. 2d surface elevation measurements by means of X-band radar. In: ninth International Workshop on Wave Hindcasting and Forecasting, Victoria, BC, Canada, pp. 1–13.

Izquierdo, P., Nieto-Borge, J.C., Guedes-Soares, C., Sanz-González, R., Rodríguez, G., 2005. Comparison of wave spectra from nautical radar images and scalar buoy data. J. Waterway Port Coastal Ocean Eng. 131 (3), 123–131.

Keller, W.C., Wright, J.W., 1975. Microwave scattering and the straining of wind-generated waves. Radio Sci. 10, 139–147.

Kimura, A., 1980. Statistical properties of random wave groups. In: 17th International Conference on Coastal Engineering, ASCE, pp. 2955–2973.

King, F.W., 2009a. Hilbert Transforms. Cambridge University Press, vol. 1.

King, F.W., 2009b. Hilbert Transforms. Cambridge University Press, vol. 2.

Krogstad, H.E., Liu, J., Socquet-Juglard, H., Dysthe, K.B., Trulsen, K., 2004. Spatial extreme value analysis of nonlinear simulations of random surface waves. In: 23rd International Conference on Offshore Mechanics and Arctic Engineering – OMAE 2004. ASME, pp. 1–11.

Krogstad, H.E., Trulsen, K., 2010. Interpretations and observations of ocean wave spectra. Ocean Dyn. 60, 973–991.

Lee, P.H.Y., Barter, J.D., Beach, K.L., Hindman, C.L., Lade, B.M., Rungaldier, H., Shelton, J.C., Williams, A.B., Yee, R., Yuen, H., 1995. X-band microwave backscattering from ocean waves. J. Geophys. Res. 100 (C2), 2591–2611.

Longuet-Higgins, M.S., 1984. Statistical properties of wave groups in a random sea state. Philos. Trans. R. Soc. London Ser. A 312, 219–250.

Longuet-Higgins, M.S., 1986. Wave Groups Statistic. In: Monahan, E.C., Niocaill, G.M. (Eds.), Oceanic whitecaps and their role in air–sea exchange processes, Springer, pp. 15–35.
Massel, S.R., 1996. Ocean Surface Waves: Their Physics and Prediction. World Scientific.
Medina, J.R., Hudspeth, R.T., 1990. A review of the analyses of ocean wave groups. Coastal Eng. 14, 515–542.
Mitsuyasu, H., Tasai, F., Suhara, T., Mizuno, S., Ohkusu, M., Honda, T, Rikiishi, K., 1980. Observation of the power spectrum of ocean waves using a cloverleaf buoy. J. Phys. Oceanogr. 10, 286–296.
Mollo-Christensen, E., Ramamonjiariosa, A., 1980. Modelling the presence of wave groups in a random wave field. J. Phys. Oceanogr. 83, 4117–4122.
Nieto-Borge, J.C., Guedes-Soares, C., 2000. Analysis of directional wave fields using X-band navigation radar. Coastal Eng. 40, 375–391.
Nieto-Borge, J.C., Hessner, K., Jarabo-Amores, P., de la Mata-Moya, D., 2008. Signal-to-noise ratio analysis to estimate ocean wave heights from X-band marine radar image time series. IET Radar Sonar Navigat. 2, 35–41.
Nieto-Borge, J.C., Lehner, S., Schulz-Stellenfleth, J., 2004a. Detection of ocean wave groupiness from spaceborne synthetic aperture radar. J. Geophys. Res. 109 (C07005), 1–18.
Nieto-Borge, J.C., Mata-Moya, D., Jarabo-Amores, P., Reichert, K., Hessner, K., 2010. Application of conventional marine radars for measuring ocean wave fields in shallow water conditions. In: IEEE International Symposium on Geoscience and Remote Sensing – IGARSS, pp. 4338–4341.
Nieto-Borge, J.C., Reichert, K., Dittmer, J., 1999. Use of nautical radar as a wave monitoring instrument. Coastal Eng. 37, 331–342.
Nieto-Borge, J.C., Rodríguez-Rodríguez, G., Hessner, K., Izquierdo-González, P., 2004b. Inversion of marine radar images for surface wave analysis. J. Atmos. Oceanic Technol. 21, 1291–1300.
Nouguier, F., Guérin, C.A., Chapron, B., 2009. choppy wave model for nonlinear gravity waves. J. Geophys. Res. 114 (C09012), 1–15.
Ochi, M.K., 2005. Ocean Waves: The Stochastic Approach. Cambridge University Press.
Onorato, M., Proment, D., Toffoli, A., 2010. Freak waves in crossing seas. Eur. Phys. J. Spec. Top. 185, 45–55.
Piotrowski, C.C., Dugan, J.P., 2002. Accuracy of bathymetry and current retrievals from airborne optical time-series imaging of shoaling waves. IEEE Trans. Geosci. Remote Sens. 40, 2606–2618.
Plant, W.J., 1990. Bragg scattering of electromagnetic waves from the air/sea interface. In: Geernaert, G.L., Plant, W.J. (Eds.), Surface Waves and Fluxes: Current Theory and Remote Sensing, vol. 2. Kluwer Academic Publishers, pp. 41–108.
Plant, W.J., Farquharson, G., 2012. Origins of features in wave number–frequency spectra of space–time images of the ocean. J. Geophys. Res. 117 (C06015), 1–10.
Reichert, K., Hessner, K., Dannenberg, J., Tränkmann, I., Lund, B., 2005. X-band radar as a tool to determine spectral and single wave properties. WAVES 2005, ASCE, pp. 1–9.
Reichert, K., Hessner, K., Nieto-Borge, J.C., Dittmer, J., Lund, B., 1999. WaMoS II: A radar based wave and current monitoring system. In: ISOPE'99 Proceedings, pp. 1–5.
Reichert, K., Lund, B., 2007. Ground based remote sensing as a tool to measure spatial wave field variations in coastal approaches. In: 9th International Coastal Symposium, Gold Coast, Queensland, Australia, pp. 1–5.
Robinson, I.S., Ward, N.P., Gommenginger, C.P., Tenorio-Gonzales, M.A., 2000. Coastal oceanography applications of digital image data from marine radar. J. Atmos. Oceanic Technol. 17 (5), 721–735.
Seemann, J., 1997. Interpretation of the structure of the frequency-wave number spectrum of nautical radar temporal sequences of sea states (in German). Ph.D. thesis, University of Hamburg.
Seemann, J., Ziemer, F., Senet, C.M., 1997. A method for computing calibrated ocean wave spectra from measurements with a nautical X-band radar. In: IEEE Oceans'97 Conference Proceedings, vol. 2, pp. 1148–1154.
Senet, C.M., Seemann, J., Ziemer, F., 2001. The near-surface current velocity determined from image sequences of the sea surface. IEEE Trans. Geosci. Remote Sens. 39, 492–505.
Sierra-Vázquez, V., Serrano-Pedraza, I., 2010. Application of Riesz transforms to the isotropic AM–PM decomposition of geometrical-optical illusion images. J. Opt. Soc. Am. 27, 781–796.
Skolnik, M.I., 2008. Radar Handbook. McGraw–Hill Professional.
Stevens, C.L., Poulter, E.M., Smith, M.J., McGregor, J.A., 1999. Nonlinear features in wave-resolving microwave radar observations of ocean waves. IEEE J. Oceanic Eng. 24 (4), 470–480.
Tayfun, A., Fedele, F., 2007. Wave-height distributions and nonlinear effects. Ocean Eng. 34, 1631–1649.
Terrill, E.J., de Paolo, A., 2009. Phase resolved measurements of ocean waves using X-band radar. In: ONR Workshop on Deterministic Measurement and Simulation of Ocean Waves, May 4–6. De Lindenhof, Delft.
Trizna, D.B., 2001. Errors in bathymetric retrievals using linear dispersion in 3D FFT analysis of marine radar ocean wave imagery. J. Geophys. Res. 39 (C7), 12529–12537.
Wu, L.C., Chuang, L.Z.H., Doong, D.J., Kao, C.C, 2011. Ocean remotely sensed image analysis using two-dimensional continuous wavelet transforms. Int. J. Remote Sens. 32 (23), 8779–8798.
Wyatt, L.R., Green, J.J., Gurgel, K.W., Nieto-Borge, J.C., Reichert, K., Hessner, K., Günther, H., Rosenthal, W., Saetra, O., Reistad, M., 2003. Validation and intercomparisons of wave measurements and models during the EuroROSE experiments. Coastal Eng. 48 (1), 1–28.
Yefimov, V.V., Babanin, A.V., 1991. Dispersion relation for the envelope of groups of wind waves. Izvestiya, Atmos. Oceanic Phys. 27 (8), 599–603.
Young, I.R., Rosenthal, W., Ziemer, F., 1985. A three-dimensional analysis of marine radar images for the determination of ocean wave directionality and surface currents. J. Geophys. Res. 90, 1049–1059.
Ziemer, F., Brockmann, C., Vaughan, R., Seemann, J., Senet, C., 2004. Radar survey of near shore bathymetry within the OROMA project. EARSeL eProc. 3 (2), pp. 282–228.
Ziemer, F., Dittmer, J., 1994. A system to monitor ocean wave fields. In: IEEE Oceans'94 Conference Proceedings, vol. 2, pp. 28–31.